

# Airborne Observations of Fetch-Limited Waves in the Gulf of Tehuantepec

LEONEL ROMERO AND W. KENDALL MELVILLE

*Scripps Institution of Oceanography, University of California, San Diego, La Jolla, California*

(Manuscript received 19 August 2008, in final form 22 July 2009)

## ABSTRACT

The authors present airborne observations of fetch-limited waves during strong offshore winds in the Gulf of Tehuantepec. The measurements, collected over a wide range of fetches, include one- and two-dimensional surface wavenumber spectra and turbulent fluxes in winds up to  $25 \text{ m s}^{-1}$ . The evolution of the wave spectra is in good agreement with the fetch relationships from previous observations. The tails of the observed one-dimensional  $k_1$  spectra, in the dominant wave direction, exhibit a  $k_1^{-3}$  power law over a wide range of wavenumbers. The authors present the first quantification of the transition between the equilibrium and saturation ranges for the omnidirectional spectrum in the wavenumber domain. The energy density within the equilibrium range shows a dependence on the wave age. At wavenumbers higher than the spectral peak, the width of the spectrum in the direction orthogonal to the dominant waves is nearly independent of the wave age. However, in the azimuthal direction, the spreading of the spectrum decreases with increasing effective wave age. The bimodal directional distribution, characterized by the lobe amplitude and separation, shows a consistent scaling with both parameters collapsing when scaled by the square root of the wave age. The one-dimensional fetch-limited  $k_1$  spectrum is well parameterized with dependence on the effective fetch and friction velocity. At higher wavenumbers within the saturation range, although the one-dimensional saturation in the dominant wave direction is independent of the wind forcing, the saturation in the crosswind direction is weakly dependent on the effective wave age and on average 30% larger than that in the downwind direction. The results are discussed in the context of previous observations and current numerical wind-wave prediction models.

## 1. Introduction

Wind waves are important for air–sea interaction, because they influence the exchange of mass, momentum, and energy between the ocean and the atmosphere (Donelan 1990; Melville 1996). As a wave field develops, the wind provides wave energy and momentum to the ocean, some of which can propagate away from the generation area in the form of swell, whereas the remainder is lost locally (primarily because of wave breaking) to generate currents and turbulence. Donelan (1998) used field measurements of wave growth (Donelan et al. 1992) and a parameterization of wind input from field and laboratory measurements (Donelan 1987) to show that less than 5% of the total energy and momentum supplied by the wind is retained by the surface waves; however, recent models suggest that at short fetches the fraction of

wave energy retained from the wind may be 10% or more (Romero and Melville 2010). Surface waves extract momentum from the atmosphere and influence the drag coefficient by supporting wave-induced stresses (Janssen 1989). For example, Banner and Melville (1976) and Banner (1990b) showed experimentally that airflow separation over steep breaking waves can enhance the momentum transfer when compared to attached flows. More recently, based on field observations, Grachev and Fairall (2001) showed that swell traveling faster than the wind may result in a momentum flux from the ocean waves to the atmosphere.

In the mid-1900s, the study of surface waves gained a lot of interest after the pioneering work by Sverdrup and Munk (1947). In the past 60 yr, the use of various observational, theoretical, and experimental investigations has resulted in a better understanding of many processes involved in the generation and evolution of surface waves (Mitsuyasu 2002). It is now possible to predict wind-sea wave heights and periods for practical applications at global scales. However, the errors among various present numerical models are significant,

---

*Corresponding author address:* Leonel Romero, Scripps Institution of Oceanography, University of California, San Diego, La Jolla, CA 92093-0230.  
E-mail: leromero@ucsd.edu

ranging between 7% and 30% for the wave height and between 25% and 40% for the period (Bidlot et al. 2007; Rascles et al. 2008). There are numerous physical processes and properties of wind waves that remain poorly understood, which include wave generation by wind, directional properties of the spectrum at finite fetch, evolution of the spectrum under high winds ( $>15 \text{ m s}^{-1}$ ), and deep-water wave breaking (WISE Group 2007).

In this study, we present the analysis of state-of-the-art wind-wave measurements collected from the National Science Foundation/National Center for Atmospheric Research (NSF/NCAR) C-130 aircraft during the Gulf of Tehuantepec Experiment (GOTEX) in February 2004. The Gulf of Tehuantepec is characterized by strong offshore winds that occur primarily during the boreal winter (Romero-Centeno et al. 2003), when cold weather systems move south into the Gulf of Mexico. This creates significant pressure differences across the Tehuantepec isthmus, with flows through a mountain gap in the Sierra Madre, forcing an offshore wind jet (known as “Tehuano”) over the Pacific Ocean.

Mesoscale numerical simulations of the Gulf of Tehuantepec by Steenburgh et al. (1998) showed a wind jet that reached a maximum speed of  $25 \text{ m s}^{-1}$  and turned anticyclonically as it emerged from the Tehuantepec isthmus. Figure 1 shows the typical structure of the fully developed wind jet from Quick Scatterometer (QuikSCAT) winds, around 1205 UTC 17 February 2004. The wind jet is narrowest and strongest near shore, with a mean orientation due south turning anticyclonically and extending out over the Pacific for 500 km or more. Schultz et al. (1998) estimated that in a typical year there are 10–12 wind events, each lasting from 2 to 6 days. Thus, the high probability and predictability of offshore wind events in the Gulf of Tehuantepec make this an ideal location to study air–sea interaction processes.

In this study, we present our analysis of the evolution of the directional wavenumber spectrum of fetch-limited waves during Tehuano conditions. Some preliminary results that focused on the incidence of extreme waves have been reported by Melville et al. (2005). In section 2, we introduce the variables and notation and provide a brief summary of other relevant wind-wave studies. In section 3, we describe the experiment, measurements, and methods used in the analysis. In section 4, we present the results, which are compared with available wind-wave observations. In section 5, we present a parameterization of the observed one-dimensional wavenumber spectra. In section 6, we discuss the results.

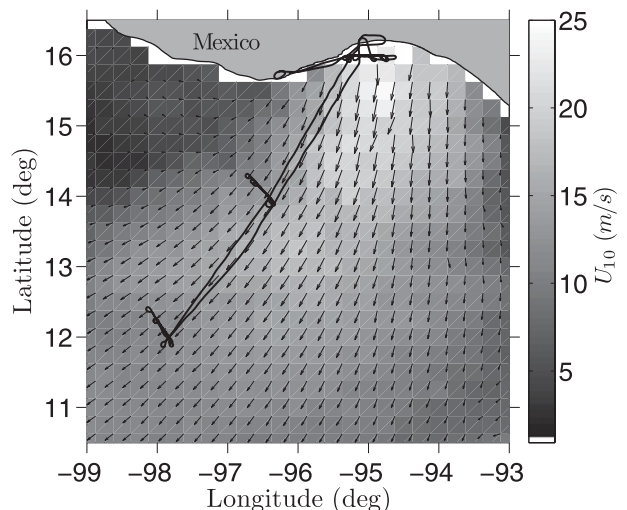


FIG. 1. QuikSCAT winds for 17 Feb 2004, showing the typical structure of the wind jet during Tehuano conditions over the Gulf of Tehuantepec. The solid black line corresponds to the flight track for research flight 05. The areas shown in white contain no data.

## 2. Background

### a. Definitions

The ocean surface elevation can be approximated to first order as a linear superposition of sinusoidal wave trains. Following Phillips (1977), for a stationary and homogeneous wave field, the ocean surface can be described in terms of the three-dimensional spectrum  $\mathcal{X}(\mathbf{k}, \omega)$ , defined as the Fourier transform of the covariance of the surface displacement  $Z(\mathbf{r}, t) = \overline{\eta(\mathbf{x}, t)\eta(\mathbf{x} + \mathbf{r}, t + \tau)}$ :

$$\mathcal{X}(\mathbf{k}, \omega) = (2\pi)^{-3} \iint Z(\mathbf{r}, t) e^{-i(\mathbf{k}\cdot\mathbf{r} - \omega\tau)} d\mathbf{r} d\tau, \quad (1)$$

where  $\eta$  is the displacement from the mean sea level,  $\mathbf{k}$  is the wavenumber vector, and  $\omega$  is the radial frequency. By definition, the integral of  $\mathcal{X}(\mathbf{k}, \omega)$  over all wavenumbers and frequencies is the variance ( $\langle \eta^2 \rangle = \iint \mathcal{X}(\mathbf{k}, \omega) d\mathbf{k} d\omega$ ), which is proportional to the sum of the potential and kinetic energy densities,  $E = \rho_w g \langle \eta^2 \rangle$ , where  $g$  is the gravitational acceleration and  $\rho_w$  is the water density.

In practice, most field observations of wind-wave spectra are limited to only measuring projections of  $\mathcal{X}(\mathbf{k}, \omega)$ . Following Banner (1990a), these include the

$$\text{frequency spectrum, } \psi(\omega) = \int_{-\infty}^{\infty} \mathcal{X}(\mathbf{k}, \omega) d\mathbf{k}; \quad (2)$$

directional frequency spectrum,

$$\varphi(\omega, \theta) = 2 \int_0^{\infty} \mathcal{X}(k, \theta, \omega) k dk; \quad (3)$$

directional wavenumber spectrum,

$$F(k, \theta) = 2 \int_0^\infty \mathcal{X}(k, \theta, \omega) d\omega; \quad (4)$$

omnidirectional wavenumber spectrum,

$$\phi(k) = \int_{-\pi}^\pi F(k, \theta) k d\theta; \quad (5)$$

$k_1$  and  $k_2$  spectra,  $\phi_1(k_1) = \int_{-\infty}^{+\infty} F(k_1, k_2) dk_2;$  and (6)

$$\phi_2(k_2) = \int_{-\infty}^{+\infty} F(k_1, k_2) dk_1, \quad (7)$$

where  $k = (k_1^2 + k_2^2)^{1/2}$  and  $\theta = \arctan(k_2/k_1)$ .

For waves obeying the linear deep-water dispersion relationship,  $\omega^2 = gk$ , the measured frequency spectra can be converted to the wavenumber domain according to

$$F(k, \theta) = \frac{1}{k} \frac{\partial \omega}{\partial k} \varphi(\omega, \theta) \quad \text{and} \quad (8)$$

$$= \frac{g^{1/2}}{2k^{3/2}} \varphi(\omega, \theta). \quad (9)$$

However, temporal point measurements (e.g., pitch and roll buoys) are greatly affected by the Doppler shift caused by the orbital motions of longer waves on the shorter waves (Kitaigorodskii et al. 1975; Phillips 1981). The computations by Banner (1990a) showed that the Doppler shift induced by steep dominant waves can significantly reduce the spectral slope at high frequencies. But the problems arising from single-point measurements can be significantly reduced by using spatial measurements such as airborne observations of the ocean surface topography, which essentially capture a snapshot of the surface wave field and are not affected at leading order by motion of the dominant waves.

*b. Previous wind-wave studies*

Because the development of wind-generated wave fields can be influenced by water depth, coastal topography, surface currents, and the spatial structure and steadiness of the wind field, the ideal conditions to study the development of a wave field are either fetch- or duration-limited (Young 1999). Fetch-limited conditions are defined as steady and homogeneous winds blowing off an infinite and straight coastline, and duration-limited conditions correspond to steady and homogeneous winds blowing over an infinite area from some initial time. Using similarity arguments, Kitaigorodskii (1962) proposed that under ideal conditions the main controlling

parameters of the wind-wave spectrum are the gravitational acceleration  $g$ ; the friction velocity  $u_*$  in the air; and the fetch  $X$  or duration, depending on the conditions. However, in practice most field observations of wind waves typically measure the horizontal surface winds and not  $u_*$ , thus relying on either bulk parameterizations of the drag coefficient (e.g., Wu 1982) or on the surface wind speed (typically at 10 m above mean sea surface,  $U_{10}$ ) as the scaling velocity for the analysis of the wind-wave spectrum.

The measurements of fetch-limited waves by Hasselmann et al. (1973), collected during the Joint North Sea Wave Project (JONSWAP), are considered a milestone in the study of wind-generated ocean waves with some of the most important outcomes being the parameterization of the frequency spectrum and the empirical fetch relationships [the so-called Sverdrup–Munk–Bretschneider (SMB) curves; Sverdrup and Munk 1947; Bretschneider 1952], which relate the dimensionless energy density  $\tilde{\epsilon} = g^2 \langle \eta^2 \rangle / U_{10}^4$  and peak frequency  $\tilde{\nu} = U_{10} f_p / g$  to the dimensionless fetch  $\tilde{\chi} = gX / U_{10}^2$ , where  $f_p$  is defined in hertz.

Since JONSWAP, several field investigations have been carried out to study the evolution of fetch-limited wind-wave spectra, primarily in the frequency domain, in wind speeds ranging from 5 to 15 m s<sup>-1</sup> (e.g., Kahma 1981; Donelan et al. 1985; Dobson et al. 1989; Donelan et al. 1992). However, the various growth rates reported had considerable scatter. Kahma and Calkoen (1992) reanalyzed various open ocean and lake observations of fetch-limited waves, including the JONSWAP data and Lake Ontario measurements by Donelan et al. (1985), and found a significant reduction in the scatter by sorting the data into stable and unstable conditions, according to the atmospheric stratification. In finite-depth conditions, Young (1998) found robust evidence that the growth rate can vary within a factor of 2 because of the influence of the atmospheric boundary layer stability. Unlike Janssen et al. (1987), Kahma and Calkoen (1992) found little change when scaling the fetch relations with  $u_*$ , which they estimated using a bulk parameterization of the drag coefficient.

More recently, Hwang et al. (2000a,b) reported on the analysis of airborne observations of directional and one-dimensional wavenumber wind-wave spectra with good directional resolution for a quasi-steady and a decaying wave field under mild forcing conditions, with wind speeds of 10 m s<sup>-1</sup>. In this study, we present similar airborne observations of directional wavenumber spectra over a wide range of fetches in strong winds, between 10 and 20 m s<sup>-1</sup>, as well as estimates of  $u_*$  from airborne turbulence measurements at an altitude between 30 and 50 m above mean sea level.

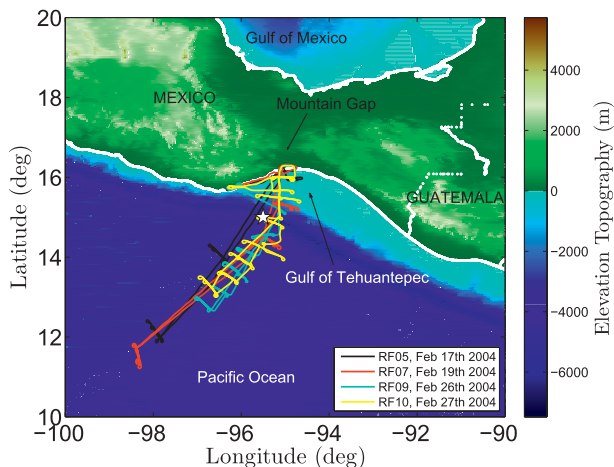


FIG. 2. GOTEX flight tracks from research flights 05, 07, 09, and 10. The white star corresponds to the location of wind time series shown in Fig. 3.

### 3. The experiment

Data were collected from the NSF/NCAR C-130 aircraft, which allows extensive spatial coverage over hundreds of kilometers in a relatively short time. The aircraft was equipped with fast response (25 Hz) instrumentation to measure the standard atmospheric variables, including the temperature, humidity, and vector winds, from which turbulent fluxes can be derived (Brown et al. 1983). The sea surface elevation was measured with two laser-based instruments, the National Aeronautics and Space Administration (NASA)/EG&G Airborne Topographic Mapper (ATM), which is a conically scanning lidar, and a fixed nadir-looking Riegl laser ranging system (model LD90-3800EHS-FLP). In this study, we present the analysis of wave-number spectra from measurements collected on 17, 19, 26, and 27 February 2004, which correspond to research flights (RFs) 05, 07, 09, and 10, with the flight tracks shown in Fig. 2.

Figure 3 shows the time history of the surface winds over the last two weeks of February 2004 at (15°N, 95.5°W) in the Gulf of Tehuantepec. The wind speed and direction were obtained from the National Centers for Environmental Prediction (NCEP) North American Regional Reanalysis (NARR) and QuikSCAT. The flight periods for RFs 05, 07, 09, and 10 are shown with solid gray lines. The time series shows two main wind events, with the strongest between 15 and 20 February and the other between 26 and 29 February. In contrast to RFs 07 and 09, which were conducted during the final and initial stages of a wind event, respectively, RFs 05 and 10 were carried out during quasi-steady wind conditions. To minimize the uncertainties associated with

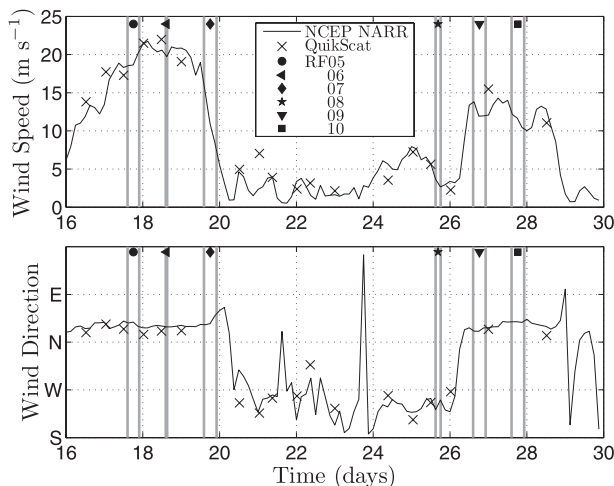


FIG. 3. Time series for February 2004 of surface wind (top) speed and (bottom) direction from model (NCEP/NARR) and scatterometer (QuikSCAT) wind products at (15°N, 95.5°W). The gray lines bound the flight periods for RFs 05, 06, 07, 08, 09, and 10.

the unsteadiness of the wind field, for RF 07 we only considered the morning measurements, which are limited to the downwind leg between the coast and the farthest point offshore, and for RF 09 we considered both morning and afternoon measurements but only within 200 km of the coast.

#### a. Sea surface topography

The ATM is a conical scanning lidar developed by NASA/EG&G, which is principally used to monitor ice sheets and glaciers in polar regions (Krabill et al. 1995). The ATM was previously deployed by Hwang et al. (2000a,b) to measure the directional properties of surface waves at Duck, North Carolina. During GOTEX, the ATM's conical scanning angle was 15° with a pulse repetition and sampling frequency  $f_s = 5$  kHz and a scanning frequency  $f_{sc} = 20$  Hz. The ATM was operated primarily at a nominal altitude of 400 m above mean sea surface. For this configuration, the radius of the scanning pattern on the sea surface  $R$  is approximately 100 m. Assuming no pulse return dropouts, the maximum horizontal separation between consecutive measurements in the along-flight direction is given by the ratio of the horizontal aircraft speed  $v_a$  to the scanning frequency  $f_{sc}$ . For the typical value of  $v_a = 100$  m s<sup>-1</sup>, the horizontal resolution in the along-flight direction is 5 m. The cross-track resolution is approximately 2.5 m, given by the ratio of the perimeter of the circular scan at the surface,  $P = 2\pi R \approx 628$ , and the number of pulses along the scan,  $N = f_s/f_{sc} = 250$ . The beam divergence of the laser is 1 mrad, which corresponds to an ocean surface footprint of 0.4 m when flying at an altitude of

400 m. According to Krabill and Martin (1987), the calibrated absolute error per pulse in the elevation measured by the ATM is 8 cm, which includes a 3-cm [root-mean-square (rms)] range error, 5 cm for positioning through differential GPS, and 5 cm for attitude-induced errors.

The fixed lidar altimeter (Riegl) provided reliable backscatter when flying at altitudes between 30 and 200 m above mean sea level. The Riegl was set to sample the ocean surface at 5 kHz and had a typical pulse return rate of approximately 65%. All available pulse returns within a time interval of 0.01 s were averaged to a single value. Thus, the effective data rate was 100 Hz, resulting in a horizontal resolution of approximately 1 m and a typical data dropout rate of about 5%. Data dropouts were filled in through linear interpolation. Because of a beam divergence of 1.6 mrad by 1.8 mrad, the Riegl footprint on the sea surface was at most 32 cm by 36 cm, which is smaller than the Nyquist wavelength of 2 m.

Before estimating the one-dimensional spectra from Riegl measurements, the aircraft motion must be removed from the raw signal. This was done following Walsh et al. (1985), in which the sea surface displacement  $\eta$  relative to the mean sea surface elevation is given by

$$\eta = h - r \cos \varphi_T - \langle h - r \cos \varphi_T \rangle \quad \text{and} \quad (10)$$

$$\varphi_T^2 = \varphi_r^2 + \varphi_p^2, \quad (11)$$

where  $h$  is the aircraft altitude;  $r$  is the lidar range;  $\varphi_r$  and  $\varphi_p$  are the pitch and roll angles, respectively; and the brackets on the right side represent an spatial average over the record length. Here,  $h$  is obtained from the differential global positioning system (DGPS) with an accuracy of  $\pm 10$  cm. The net rms elevation error is approximately 11 cm, which includes the Riegl's range accuracy of 5 cm and the DGPS uncertainty.

The spatial profiles of the sea surface elevation obtained from the Riegl measurements were approximately aligned with or perpendicular to the mean wind direction, giving one-dimensional  $k_1$  and  $k_2$  spectra with respect to the wind. The wavenumber spectrum was estimated using standard Fourier transform techniques from spatial series 5 km long tapered with a Hann window. The Doppler shift induced in the  $k_1$  spectra resulting from the relative motion between the waves and the aircraft was corrected as described in section 3b.

### b. Directional wavenumber spectra

The ATM data along the circular scanning pattern on the surface of the ocean were separated into forward and rear scans, and each data subset was binned in a hori-

zontal spatial grid of 5 m by 5 m. Because the typical dropout rate was approximately 30%, yielding an effective sampling rate of 3.5 kHz, available pulses within each cell were averaged together and empty cells were interpolated from neighboring points using a two-dimensional Gaussian interpolator with an isotropic decorrelation length scale of 10 m. Figure 4 shows a sample ATM sea surface topography interpolated on a regular grid from measurements collected during RF05 at various fetches. Note the increase in the dominant wavelength with increasing fetch.

Once the data were gridded and interpolated on a regular grid, the directional spectrum was computed from the two-dimensional FFT over typical data segments 200 m wide by 5000 m long. Before Fourier transforming, data were detrended, tapered with a two-dimensional Hann window dynamically adjusted to match the meandering of the ATM swaths, and padded with zeros such that the total number of nodes was  $64 \times 1024$  with spectral resolutions  $dk_y = 2\pi/320 = 0.0196 \text{ rad m}^{-1}$  and  $dk_x = 2\pi/5120 = 0.0012 \text{ rad m}^{-1}$  in the cross-track and along-track directions, respectively. Following Walsh et al. (1985), each spectrum was corrected iteratively for the Doppler shift induced because of the relative motion between the phase speed of the waves  $c$  and the aircraft velocity, assuming the linear dispersion relationship. The change in wavenumber component  $\delta k_x$  in the along-track direction is given by the ratio of the wave frequency to the aircraft velocity,

$$\delta k_x = \frac{\omega}{v_a}, \quad (12)$$

where  $\omega^2 = gk \tanh(kh)$ , according to the linear dispersion relation. Thus, in deep water, the relative shift  $\delta k_x/k = c/v_a$  is greater for longer waves, because their speeds become a nonnegligible fraction of the aircraft velocity. In this study, we used the ocean-floor bathymetry product by Smith and Sandwell (1997), but our measurements are effectively in deep water, because the continental slope drops off very steeply within the gulf.

For consistency in the analysis, a number of spectra were averaged together so that the total distance covered by each spectrum contains approximately 150 dominant waves at all fetches. In addition, each average spectrum was smoothed with a two-dimensional Gaussian filter so that the total number of degrees of freedom (DOFs) was the same (480) for all spectra used in the analysis. Thus, the uncertainty at the 95% confidence interval corresponds to 25% of the spectral variance (Young 1995). Finally, all spectra were rotated so that the unit vector  $\mathbf{k}_1$  corresponds to the direction of the dominant waves, which was typically within a few degrees of the mean wind direction. For all the directional

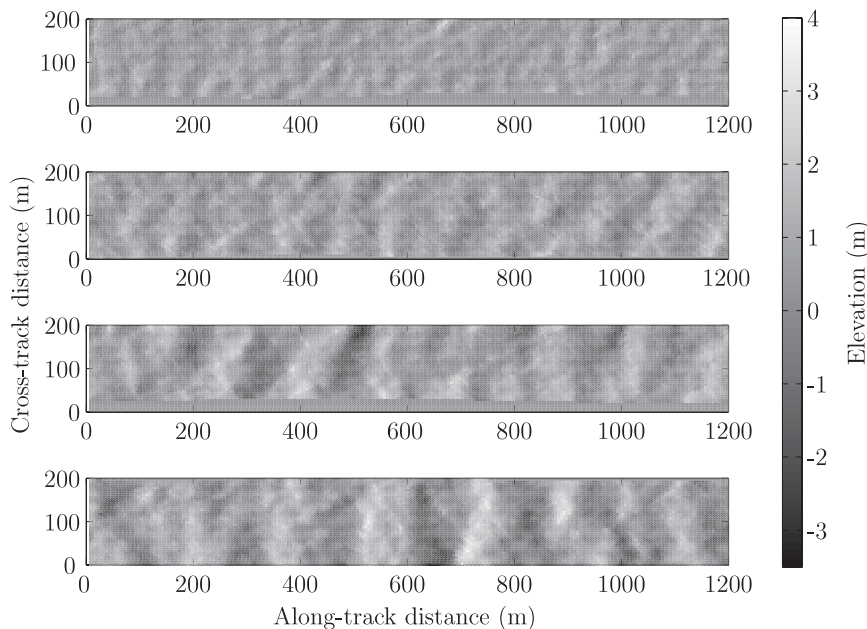


FIG. 4. Typical ATM sea surface topography measurements collected during RF 05 at fetches of (top)–(bottom) 24, 64, 205, and 345 km. Note the increase in the dominant wavelength with increasing fetch.

spectra analyzed, the difference between the dominant wave direction and the wind had a mean value of  $11^\circ$  and a standard deviation of  $12^\circ$ , implying that the dominant waves are on average to the right of the wind. In this study, the directional spectra analyzed correspond to measurements from either downwind or upwind flight tracks, except for one spectrum, which was obtained from crosswind measurements. Figures 5 and 6 show the typical development of two-dimensional wavenumber spectra of the sea surface elevation and slope, respectively, with increasing fetch.

From visual examinations of the one-dimensional  $k_1$  and  $k_2$  spectra, the upper limits before reaching the noise floor were determined to be  $0.35$  and  $0.5 \text{ rad m}^{-1}$ , corresponding to wavelengths of  $18.0$  and  $12.6 \text{ m}$  for the  $k_1$  and  $k_2$  components, respectively. These values are reasonable considering the occasional dropout segments along the scan (see, e.g., Fig. I.4 of Romero 2008).

The azimuthal directional resolution  $d\theta$  of the measured spectra in the  $(k_1, k_2)$  plane with spectral resolutions  $dk_1$  and  $dk_2$ , respectively, corresponds to

$$d\theta = \frac{dk_1 dk_2}{k dk}. \quad (13)$$

Setting  $dk = dk_1$ , the directional resolution becomes

$$d\theta = \frac{dk_2}{k}. \quad (14)$$

From Eq. (14) and the corresponding directional resolutions for the range of measured spectral peak wavenumbers (i.e., from  $0.05$  to  $0.25 \text{ rad m}^{-1}$ ) and the upper limit of  $0.35 \text{ rad m}^{-1}$ , the corresponding directional resolutions are  $22.5^\circ$ ,  $4.5^\circ$ , and  $3.2^\circ$ , respectively. Thus, for short dominant waves our measurements have good directional resolution with little information about the tail of the spectrum. Conversely, the spectra of long dominant waves have less directional resolution at the peak but cover a wide range of scales within the tail.

The circular ATM scanning pattern (see Fig. I.4 of Romero 2008) results in a temporal lag between the sampling points in the cross-track direction. Although approximately 87% of the data have time lags of  $0.5 \text{ s}$  or less, the lag between the data in the central region and the edge of the swath is approximately  $1 \text{ s}$  (Hwang et al. 2000a). To assess the impact of the time lag on the directional spreading of the measured spectra, we assume the linear dispersion relation to estimate the spatial lag between the central region and the edge of the swath. Considering both limits of the range of dominant waves resolved,  $0.05$  to  $0.25 \text{ rad m}^{-1}$ , and the upper limit of  $0.35 \text{ rad m}^{-1}$  before the noise floor, the spatial lags  $\delta x$  between the center and edge of the swath over  $1 \text{ s}$  are  $14$ ,  $6.3$ , and  $5.3 \text{ m}$ , respectively, which correspond to azimuthal errors  $\delta\theta = \delta x/100$  of about  $8^\circ$ ,  $3.6^\circ$ , and  $3^\circ$ , respectively. For the range of wavenumbers resolved,  $\delta\theta$  is always less than  $d\theta$ ; thus, the effect of the time lag on the directional spreading is expected to be small.

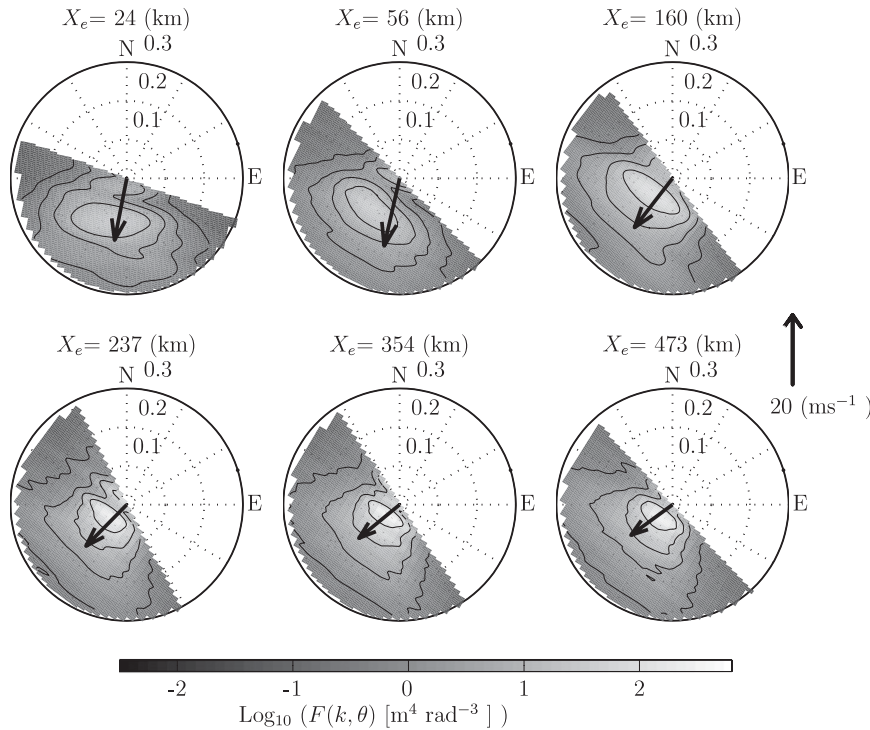


FIG. 5. Typical directional wavenumber spectra of the sea surface elevation  $F(k, \theta)$  for RF 05. The corresponding fetches are 24, 56, 160, 240, 354, and 473 km. The black arrows correspond to the surface wind vectors  $(U_{10}, \theta_w)$ .

*c. Surface winds and friction velocity*

The instantaneous wind velocities measured by the aircraft are decomposed into the mean and fluctuating components

$$u = U + u', \tag{15}$$

$$v = V + v', \text{ and} \tag{16}$$

$$w = W + w', \tag{17}$$

where  $u, v,$  and  $w$  correspond to the two horizontal and vertical velocity components, respectively, and  $U, V,$  and  $W$  correspond to the temporal average of each component, which translates to a spatial average resulting from the horizontal motion of the aircraft. The wind stress  $\tau$  can be directly obtained from the horizontal Reynolds stresses

$$\tau = \rho u_*^2 = \rho \sqrt{\langle u'w' \rangle^2 + \langle v'w' \rangle^2}, \tag{18}$$

where  $\rho$  is the air density and the angle brackets correspond to temporal averages. In this study, all estimates of  $u_*$  are from time averages of 50 s, which correspond to spatial averages over approximately 5 km. In this study, we only consider the estimates of  $u_*$  collected

from the lowest-altitude runs, typically at approximately 40 m above mean sea level, except for RF 05, when the low-altitude runs were around 50 m.

The wind profile below the aircraft can be estimated by

$$U(z) = \frac{u_*}{\kappa} \left[ \ln \frac{z}{z_o} - \Psi \left( \frac{z}{L} \right) \right], \tag{19}$$

where  $\kappa = 0.4$  is von Kármán's constant;  $z_o$  is the roughness length;  $\Psi(z/L)$  is an empirical stratification function;  $L$  is the Monin–Obukhov length,

$$L = \frac{-u_*^3 \Theta_v}{\kappa g \langle w' \theta'_v \rangle}; \tag{20}$$

and  $\Theta_v$  and  $\theta'_v$  are the mean and fluctuating virtual potential temperatures, respectively (Jones and Toba 2001).

Under stable stratification  $zL^{-1} > 0,$

$$\Psi \left( \frac{z}{L} \right) = 2 \ln \left( \frac{1 + \Phi_m^{-1}}{2} \right) + \ln \left( \frac{1 + \Phi_m^{-2}}{2} \right) - 2 \tan^{-1}(\Phi_m^{-1}) + \frac{\pi}{2}, \tag{21}$$

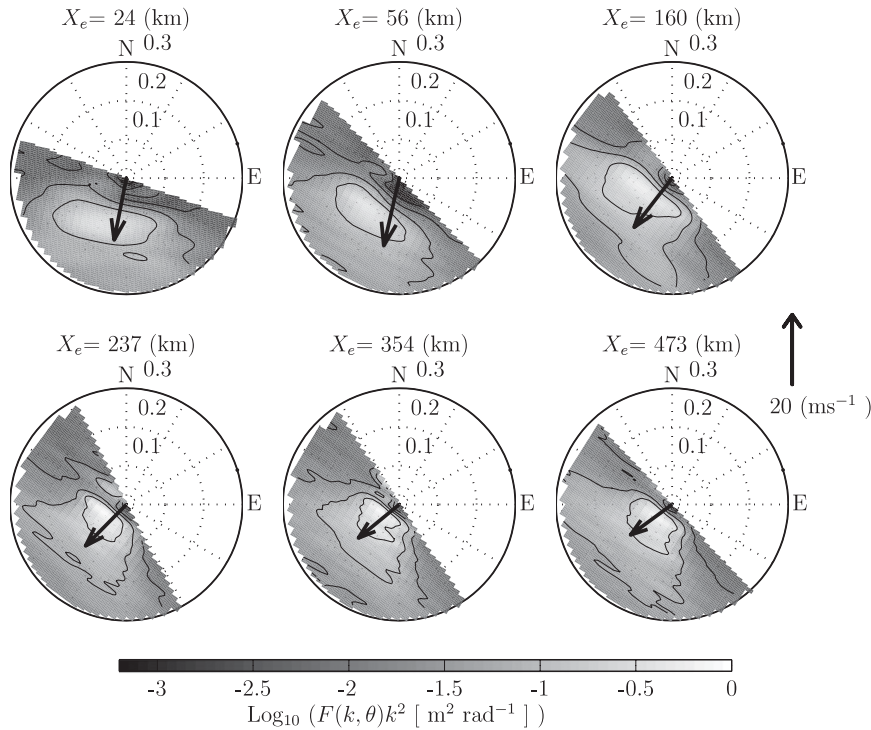


FIG. 6. As in Fig. 5, but for sea surface slope  $F(k, \theta)k^2$ .

where  $\Phi_m = (1 - c^- z/L)^{-1/4}$  and  $c^- \sim 17$ . For unstable conditions,  $zL^{-1} < 0$ ,

$$\Psi\left(\frac{z}{L}\right) = -c^+ \frac{z}{L}, \quad (22)$$

where  $c^+ \sim 4.5$  (Jones and Toba 2001).

For neutral conditions  $L = \infty$  and  $\Psi = 0$ , thus the equivalent neutral wind is defined as

$$U_N(z) = \frac{u_*}{\kappa} \ln \frac{z}{z_o}. \quad (23)$$

Using Eq. (19), the wind speed at 10 m above mean sea level  $U_{10}$  can be obtained from measurements of  $U(z_r)$ ,  $u_*$ , and  $L$  at a reference level  $z_r$ :

$$U_{10} = U(z_r) + \frac{u_*}{\kappa} \left[ \ln \frac{10}{z_r} + \Psi\left(\frac{z_r}{L}\right) - \Psi\left(\frac{10}{L}\right) \right]. \quad (24)$$

The vertical wind profile in Eq. (24) is based on the assumption of spatial homogeneity and temporal stationarity and no stress divergence,  $\partial\tau/\partial z = 0$ . The momentum budget on the GOTEX measurements reported by Friehe et al. (2006) showed that the flux divergence was significant near shore (nearly balanced by the pressure gradient) but small at long fetches. However, in this study,

the stress divergence will be neglected, because extrapolation of wind stress between 30 to 10 m above mean sea level, based on the stress divergence estimates between 30 and 800 m reported by Friehe et al. (2006), would only increase the stress by about 10%, which is small compared to the 35% rms error of the measured stress divergence.

#### 4. The evolution of the wind-wave spectrum

##### a. Integral parameters

Turning and spatially inhomogeneous winds, with speeds in the range of 10–20  $\text{m s}^{-1}$ , in the presence of opposing swell make the Gulf of Tehuantepec an interesting place to study the evolution of fetch-limited waves. This section provides a brief summary of previous wind-wave studies, followed by our findings on the analysis of the evolution of the integral parameters  $\langle \eta^2 \rangle$  and the peak frequency  $f_p$  with respect to the fetch and measured friction velocity. In this study,  $f_p$  was estimated from the peak wavenumber  $k_p$  using the linear dispersion relationship for deep-water waves and  $\langle \eta^2 \rangle$  was computed only over the wind-sea part of the spectrum. The energy of the opposing swell was filtered out using a threshold on the one-dimensional saturation  $B_1 = \phi_1(k_1)k_1^3$  by finding the lowest wavenumber component  $k_s$  where  $B_1$  is just below the threshold value

$B_{1_{\text{sea}}} = 3 \times 10^{-4}$  (Fig. A1 shows sample spectra and their respective values of  $k_s$ ).

To our knowledge, no field study to date has found a significant effect on the overall evolution of the fetch-limited wind waves in the presence of swell. Kahma and Calkoen (1992) found essentially no change in the wave growth observed for datasets with or without the presence of swell. Field studies by Dobson et al. (1989), Violante-Carvalho et al. (2004), and more recently by Ardhuin et al. (2007) did not find a significant effect of the opposing swell on the evolution of waves with fetch. In contrast, laboratory experiments by Donelan (1987) reported reduced growth rates when paddle-generated waves were imposed in the direction of the wind. Ardhuin et al. (2007) suggest that the larger steepness of the paddle-generated waves in the laboratory experiments when compared to the smaller steepness of ocean swell could account for the reduced growth rates observed by Donelan (1987).

The issues associated with inhomogeneous winds and slant fetches (winds not orthogonal to the coastline) have been addressed in other studies. Donelan et al. (1985) obtained measurements in Lake Ontario using a wave gauge array under fetch-limited conditions and avoided the effects of both inhomogeneous winds and slant fetch by fitting the wave growth and frequency downshift versus  $U_e/c_p$ , where  $c_p$  corresponds to the phase speed of the dominant waves and the effective wind speed  $U_e$  is the surface wind component in the dominant wave direction:  $U_e = U_{10} \cos(\theta_w - \theta_p)$ , where  $U_{10}$  is the surface wind speed at 10 m above mean sea level,  $\theta_w$  is the wind direction, and  $\theta_p$  is the direction of the dominant waves. Perrie and Toulany (1990) proposed the use of the effective friction velocity  $u_{*e} = u_* \cos(\theta_w - \theta_p)$  as the scaling velocity for the evolution of the energy and peak frequency of fetch-limited waves. Another way to account for spatial changes in wind speed was introduced by Dobson et al. (1989), using an average wind speed as the velocity scaling parameter for the fetch relationships:

$$\bar{U}_{10} = \frac{1}{X} \int_0^X U_{10}(X) dX. \quad (25)$$

Donelan et al. (1992) derived an empirical model for the growth rate from a fetch-dependent wind speed. For a wind speed increasing with fetch, the model predicts a reduced growth rate at short fetches (compared to a constant wind speed) but still reaches the limiting value for a Pierson–Moskowitz spectrum for fully developed seas.

For this study, the evolution of the spectral integral parameters is analyzed as follows: Because the wind and

ATM measurements were collected at different flight altitudes not coincident in space and time, the measurements of  $u_*$  from low-altitude flight tracks, typically 30 m above mean sea level, were interpolated onto the ATM sampling locations. For each pair of available directional spectra, the distance between the sampling locations  $dX$  and the average direction of the wind and dominant waves were estimated. Here,  $u_*$  and  $dX$  are projected along the dominant wave direction, corresponding to the local effective friction velocity and the effective displacement  $dX_e = dX \cos(\theta_X - \theta_p)$ , where  $\theta_X$  is the orientation of  $dX$ . The fetch-averaged effective friction velocity  $\bar{u}_{*e}$  is estimated by

$$\bar{u}_{*e_j} = \frac{1}{X_{e_j}} \sum_{i=0}^j u_{*e_i} dX_{e_i}, \quad (26)$$

where the net effective fetch  $X_{e_j} = \sum_{i=0}^j dX_{e_i}$  and the index  $i$  corresponds to the observation number ordered with increasing fetch (e.g.,  $i = 0$  is the observation closest to the coast). Tables 1 and 2 show the various wind and wave parameters of the directional spectra used in the analysis for RFs 05, 07, 09, and 10. The maximum values of  $u_{*e}$  were observed during RF 05 when the maximum surface winds, 50 m above mean sea level, reached  $25 \text{ m s}^{-1}$ . Figure 7 shows the dimensionless energy and peak frequency versus the dimensionless effective fetch. Although we are measuring the spectral peak wavenumber, we plot the peak frequency for convenience, because previous measurements were collected in the frequency domain. Figures 7a,b show  $\bar{\varepsilon} = \langle \eta^2 \rangle g^2 / \bar{u}_{*e}^4$  and  $\bar{\nu} = f_p \bar{u}_{*e} / g$ , respectively, against  $\bar{\chi} = X_e g / \bar{u}_{*e}^2$ , where  $f_p$  is in hertz. Similarly, Figs. 7c,d show  $\varepsilon = \langle \eta^2 \rangle g^2 / u_{*e}^4$  and  $\nu = f_p u_{*e} / g$ , respectively, against  $\chi = X_e g / u_{*e}^2$ . The scatter of the data is reduced when  $u_{*e}$  is used as the scaling velocity. The observed energy growth rates, regardless of the scaling velocity, are in agreement with the reanalysis by Kahma and Calkoen (1992) for stable atmospheric stratification. Most of the wind and wave measurements during GOTEX were obtained during stable conditions at short to intermediate fetches because of the strong upwelling and entrainment of cooler surface waters from below.

The power-law fits shown in Fig. 7 are

$$\bar{\varepsilon} = 4.1 \times 10^{-3} \bar{\chi}^{0.74}, \quad (27)$$

$$\bar{\nu} = 0.22 \bar{\chi}^{-0.22}, \quad (28)$$

$$\varepsilon = 1.6 \times 10^{-3} \chi^{0.81}, \quad \text{and} \quad (29)$$

$$\nu = 0.28 \chi^{-0.23}. \quad (30)$$

TABLE 1. Wind and wave conditions for RFs 05 and 07. The time is given in UTC,  $X_e$  is the effective fetch,  $U_{10}$  is the wind speed at 10-m elevation,  $u_*$  is the friction velocity,  $\theta_w$  is the wind direction,  $\theta_p$  is the dominant wave direction,  $u_{*e}$  is the effective  $u_*$ ,  $\bar{u}_{*e}$  is the fetch-averaged  $u_{*e}$ , and  $k_p$  is the spectral peak wavenumber.

Dataset	Time (UTC)	Lat (°)	Lon (°)	$X_e$ (km)	$U_{10}$ (m s <sup>-1</sup> )	$u_*$ (m s <sup>-1</sup> )	$\theta_w$ (°)	$\theta_p$ (°)	$u_{*e}$ (m s <sup>-1</sup> )	$\bar{u}_{*e}$ (m s <sup>-1</sup> )	$k_p$ (rad m <sup>-1</sup> )	$\langle \eta^2 \rangle$ (m <sup>2</sup> )
RF 05												
1	1513:43	16.12	-95.14	7	18.14	0.747	8	7	0.746	0.746	0.265	0.056
2	1514:02	16.07	-95.14	12	18.13	0.747	9	12	0.746	0.746	0.191	0.119
3	1514:57	16.03	-95.13	17	18.11	0.748	10	17	0.742	0.745	0.142	0.201
4	1515:53	15.96	-95.13	24	18.09	0.748	11	21	0.736	0.743	0.133	0.235
5	1517:01	15.87	-95.14	33	18.06	0.749	13	27	0.726	0.738	0.118	0.337
6	1518:07	15.82	-95.18	40	18.04	0.75	14	40	0.674	0.727	0.098	0.352
7	1519:27	15.74	-95.23	51	18.01	0.751	16	41	0.68	0.717	0.088	0.369
8	1521:12	15.63	-95.3	63	17.97	0.753	18	61	0.556	0.686	0.079	0.425
9	1539:03	14.48	-95.98	198	17.3	0.647	41	53	0.633	0.649	0.054	0.778
10	1541:53	14.33	-96.08	217	17.18	0.659	42	53	0.646	0.649	0.059	0.784
11	1558:25	13.34	-96.69	336	15.44	0.723	49	53	0.721	0.675	0.069	0.967
12	1600:05	13.19	-96.79	354	15.16	0.681	50	56	0.677	0.675	0.044	0.881
13	1604:01	13.02	-96.93	378	14.8	0.625	52	47	0.623	0.671	0.049	0.923
14	1607:08	12.85	-97.08	402	14.45	0.571	54	56	0.571	0.665	0.054	0.979
15	1734:27	12.41	-97.55	473	14.8	0.515	54	48	0.513	0.642	0.059	0.82
16	1754:01	13.21	-96.97	358	17.53	0.644	48	65	0.617	0.707	0.044	0.898
17	1757:08	13.32	-96.89	346	17.34	0.633	48	54	0.63	0.71	0.064	0.79
18	1917:21	14.23	-96.27	231	16.68	0.84	44	63	0.799	0.748	0.064	0.757
19	1935:34	14.96	-95.85	154	17.86	0.721	38	55	0.688	0.724	0.069	0.64
20	1938:25	15.07	-95.79	141	17.99	0.773	35	58	0.711	0.727	0.064	0.606
21	1955:51	15.75	-95.39	65	19.75	0.892	18	52	0.741	0.744	0.088	0.406
22	1959:02	15.88	-95.31	50	19.88	0.862	13	46	0.72	0.744	0.118	0.276
23	2000:08	15.92	-95.28	45	19.92	0.852	11	47	0.688	0.747	0.147	0.238
24	2001:58	15.99	-95.24	35	19.99	0.834	8	30	0.772	0.772	0.157	0.195
25	2011:01	16.12	-95	9	20.35	0.747	353	11	0.71	0.71	0.187	0.141
RF 07												
1	1459:33	16.13	-95.13	6	15.98	0.612	3	25	0.57	0.57	0.287	0.012
2	1500:12	16.09	-95.13	11	16.07	0.602	4	22	0.572	0.57	0.251	0.038
3	1500:51	16.04	-95.13	15	16.1	0.552	4	19	0.533	0.559	0.191	0.056
4	1501:03	16	-95.13	20	15.74	0.582	6	22	0.559	0.559	0.166	0.089
5	1502:09	15.95	-95.13	25	15.57	0.586	7	20	0.569	0.561	0.147	0.107
6	1502:47	15.91	-95.13	29	15.44	0.585	7	29	0.545	0.558	0.145	0.13
7	1503:49	15.84	-95.14	37	15.27	0.581	9	28	0.549	0.557	0.124	0.171
8	1505:06	15.75	-95.17	47	15.06	0.572	11	29	0.545	0.554	0.104	0.212
9	1506:41	15.64	-95.21	59	14.84	0.561	13	27	0.544	0.552	0.092	0.265
10	1524:12	14.5	-95.5	189	13.35	0.464	28	17	0.455	0.485	0.064	0.445
11	1526:46	14.33	-95.54	209	13.08	0.468	30	27	0.468	0.483	0.062	0.515
12	1546:03	13.46	-96.42	343	11.78	0.431	41	42	0.431	0.463	0.057	0.494
13	1610:12	12.44	-97.56	509	11.41	0.41	53	56	0.409	0.445	0.051	0.41

Although the measurements cover a wide range of nondimensional fetches, most of the data are concentrated at intermediate fetches. For RFs 07 and 10,  $\varepsilon$  and  $\nu$  exceed the Pierson–Moskowitz limits (Komen et al. 1984), reaching the limiting values for fully developed seas reported in the reanalysis by Alves et al. (2003).

As commented by one of the reviewers of the article, because the wave growth rate is expected to be proportional to the wind stress (i.e., friction velocity squared), Eq. (26) should integrate the friction velocity squared to obtain the fetch-averaged stress. However, the calculations of the fetch-averaged mean and root-mean-

square friction velocity gave nearly identical values, with a mean absolute difference of 0.25%.

### b. One-dimensional spectra

Figures 8a,b show the typical evolution of  $\phi(k)$  and  $\phi_1(k_1)$ , respectively, with increasing nondimensional fetch. Both sets of omnidirectional and one-dimensional spectra show a peak followed by regions exhibiting power-law behaviors, approximately proportional to  $k^{-5/2}$  and  $k_1^{-3}$ , respectively. The region immediately after the spectral peak of  $\phi(k)$  is commonly referred to as the equilibrium range.

TABLE 2. As in Table 1, but for RFs 09 and 10.

Dataset	Time (UTC)	Lat (°)	Lon (°)	$X_e$ (km)	$U_{10}$ (m s <sup>-1</sup> )	$u_{*e}$ (m s <sup>-1</sup> )	$\theta_w$ (°)	$\theta_p$ (°)	$u_{*e}$ (m s <sup>-1</sup> )	$\bar{u}_{*e}$ (m s <sup>-1</sup> )	$k_p$ (rad m <sup>-1</sup> )	$\langle \eta^2 \rangle$ (m <sup>2</sup> )
RF 09												
1	1527:08	15.79	-95.26	65	18.01	0.718	17	44	0.642	0.642	0.113	0.249
2	1528:25	15.72	-95.31	75	18.1	0.691	24	47	0.635	0.641	0.103	0.215
3	1529:43	15.64	-95.36	85	17.74	0.639	29	41	0.626	0.639	0.098	0.252
4	1531:21	15.54	-95.42	97	15.99	0.583	30	45	0.563	0.63	0.103	0.294
5	1606:41	15.03	-95.16	144	16.68	0.69	23	16	0.686	0.648	0.064	0.678
6	1609:46	14.8	-95.14	168	16.02	0.668	26	12	0.649	0.648	0.059	0.655
7	1650:27	14.37	-95.46	228	16.05	0.692	29	34	0.689	0.659	0.049	0.783
8	1653:02	14.2	-95.53	247	15.14	0.634	32	39	0.629	0.657	0.074	0.796
9	1732:33	13.96	-95.8	285	14.37	0.595	35	30	0.593	0.648	0.049	0.777
10	2124:12	15.87	-95.32	55	17.55	0.688	17	47	0.592	0.592	0.113	0.215
11	2125:27	15.78	-95.31	62	17.77	0.694	20	38	0.659	0.599	0.098	0.298
RF 10												
1	1523:45	15.9	-95.14	32	17.08	0.628	3	34	0.543	0.543	0.125	0.18
2	1525:02	15.81	-95.13	40	17.22	0.65	5	28	0.596	0.554	0.106	0.246
3	1526:19	15.72	-95.12	49	17.37	0.671	6	23	0.642	0.57	0.101	0.303
4	1527:53	15.61	-95.13	62	17.54	0.698	7	9	0.698	0.596	0.089	0.392
5	1611:44	15.39	-95.14	85	18.19	0.772	10	16	0.767	0.643	0.074	0.564
6	1613:35	15.26	-95.13	99	18	0.756	11	18	0.75	0.658	0.067	0.725
7	1615:48	15.1	-95.13	116	17.76	0.736	13	11	0.735	0.669	0.061	0.799
8	1701:34	14.6	-95.11	170	16.42	0.693	18	8	0.683	0.674	0.049	0.738
9	1754:00	14.16	-95.63	242	14.34	0.598	35	34	0.598	0.651	0.052	0.658
10	1756:33	14	-95.71	261	14.17	0.603	36	44	0.597	0.647	0.054	0.704
11	1843:49	13.68	-95.84	299	13.57	0.55	39	34	0.548	0.635	0.048	0.586
12	1847:07	13.51	-96	323	13.31	0.524	41	30	0.515	0.626	0.049	0.63
13	1929:04	13.33	-96.27	358	13.5	0.487	47	44	0.486	0.612	0.051	0.666
14	1933:01	13.18	-96.44	383	13.03	0.463	48	46	0.463	0.602	0.048	0.724
15	2133:56	15.91	-95.31	35	14.32	0.499	24	47	0.459	0.459	0.182	0.074
16	2134:36	15.87	-95.3	40	14.36	0.516	23	23	0.516	0.465	0.166	0.075
17	2135:56	15.78	-95.29	46	14.45	0.549	23	45	0.509	0.471	0.128	0.168
18	2136:36	15.73	-95.29	50	14.5	0.566	23	43	0.533	0.475	0.129	0.158

An equilibrium range with  $\phi(k) \propto k^{-5/2}$  has been consistently reported in analytical, observational, and numerical studies of wind waves. By assuming an isotropic spectrum for a range of frequencies that maintain a constant flux of energy with energy input and dissipation at low and high frequencies, respectively, Zakharov and Filonenko (1967) derived a Kolmogorov solution for weakly nonlinear waves where the frequency spectrum is proportional to  $\omega^{-4}$  [or  $\phi(k) \propto k^{-5/2}$  according to the linear dispersion relationship for deep-water waves]. The model of the equilibrium range by Phillips (1985), which assumes that the nonlinear energy flux, wind forcing, and dissipation resulting from whitecapping are in balance, proportional, and of comparable magnitude, also predicts  $\phi \propto k^{-5/2}$ . Donelan et al. (1985), using a wave gauge array in Lake Ontario, reported an equilibrium range of the frequency spectrum  $\propto \omega^{-4}$ . The reanalysis of the JONSWAP data by Battjes et al. (1987) showed that the measured spectra are better approximated with a tail of  $\omega^{-4}$ . More recently, Hwang et al. (2000a), based on airborne observations similar to those

presented in this study, reported an equilibrium range where  $\phi \propto k^{-5/2}$ . Moreover, numerical investigations have also shown that, in the absence of external forcing, there is a region of the spectrum that persistently evolves toward a power law proportional to  $k^{-5/2}$  (or  $\omega^{-4}$ ), regardless of the initial conditions (Onorato et al. 2002; Dysthe et al. 2003; Badulin et al. 2005).

Following Toba (1973), the equilibrium range can be defined as

$$\phi(k) = \frac{\beta}{2} u_* g^{-1/2} k^{-5/2}, \quad (31)$$

where  $\beta$  is an empirical parameter, often referred to as ‘‘Toba’s constant,’’ because early wave studies did not find a systematic trend with wave age (see, e.g., the summary by Phillips 1985). Resio et al. (2004) proposed an alternative scaling for Eq. (31), by introducing a weak dependence on the wave phase speed at the spectral peak,

$$\phi(k) = \frac{\alpha_4}{2} [u_a \left(\frac{c_p}{u_a}\right)^{1/3} - u_o] g^{-1/2} k^{-5/2}, \quad (32)$$

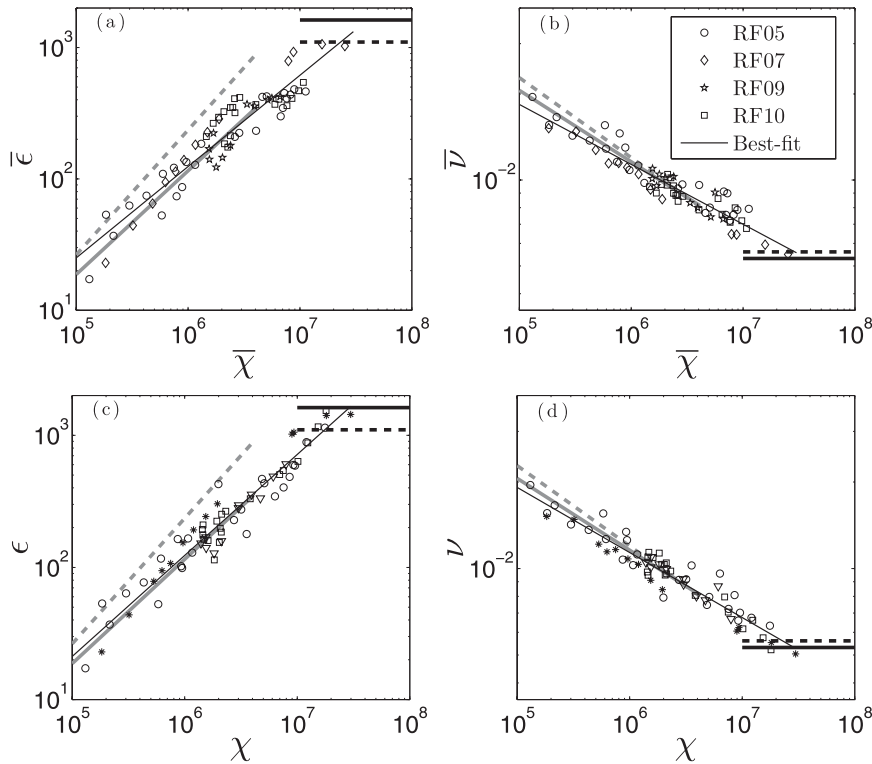


FIG. 7. (a) Nondimensional energy and (b) peak frequency vs nondimensional fetch for RFs 05, 07, 09, and 10. The scaling velocity is the fetch-averaged effective friction velocity  $\bar{u}_{*e}$  calculated according to Eq. (26). (c),(d) As in (a),(b), but with the scaling velocity corresponding to the local effective friction velocity  $u_{*e}$ . The solid gray line (gray dashed line) shows the empirical curves from Kahma and Calkoen (1992) for stable (unstable) atmospheric stratification. The limits for fully developed seas for a Pierson–Moskowitz spectrum (see Komen et al. 1984) and by Alves et al. (2003) are shown in black as solid and dashed lines, respectively.

where  $u_a$  is the scaling velocity—either  $u_*$ ,  $U_{10}$ , or  $U_\lambda$ , where  $U_\lambda$  is the wind velocity referenced to a height proportional to the wavelength at the spectral peak. The term  $u_o$  is a small scaling velocity below which Eq. (32) is no longer valid. Resio et al. (2004) found a better agreement relating the equilibrium range to both the scaling velocity and peak wavenumber than to the scaling velocity alone.

Figure 9a shows Toba's parameter against the effective wave age ( $c_p/u_{*e}$ ), showing an increasing trend with increasing wave age. The range of values observed are in good agreement with those previously reported from measurements of frequency spectra, as summarized by Phillips (1985), where  $0.06 < \beta < 0.11$  (shown with dashed lines). The best power-law fit gives

$$\beta = 0.016 \left( \frac{c_p}{u_{*e}} \right)^{0.53 \pm 0.02}, \quad (33)$$

where the uncertainty corresponds to the 95% confidence interval. The open squares are bin averages of  $\beta$

obtained by combining Eqs. (31) and (32) by using the best-fit estimates of  $\alpha_4 = 0.0459$  and  $u_o = 0.291 \text{ m s}^{-1}$  by Resio et al. (2004), with scaling velocity  $u_a = u_*$ , and our measurements of  $k_p$  and  $u_{*e}$ , assuming that  $u_* = u_{*e}$ . The GOTEX measurements of  $\beta$  are lower than those by Resio et al. (2004), with larger discrepancies toward lower values of  $c_p/u_{*e}$ . However, the data are in good agreement with Hwang et al. (2000a) near full development (open star). The dashed–dotted line with error bars corresponds to the mean and standard deviation of  $\beta$  from the reanalysis of the JONSWAP data by Battjes et al. (1987), showing on average larger values than the observations from GOTEX. Finally, using the scaling of the equilibrium range by Resio et al. (2004), according to Eq. (A2), Fig. 10 also shows that the GOTEX measurements are lower on average than Resio et al. (2004) but mostly within the range of values they reported.

Figure 11 shows a comparison of one-dimensional wavenumber spectra estimated from ATM and Riegl measurements collected within 50 km of each other at fetches

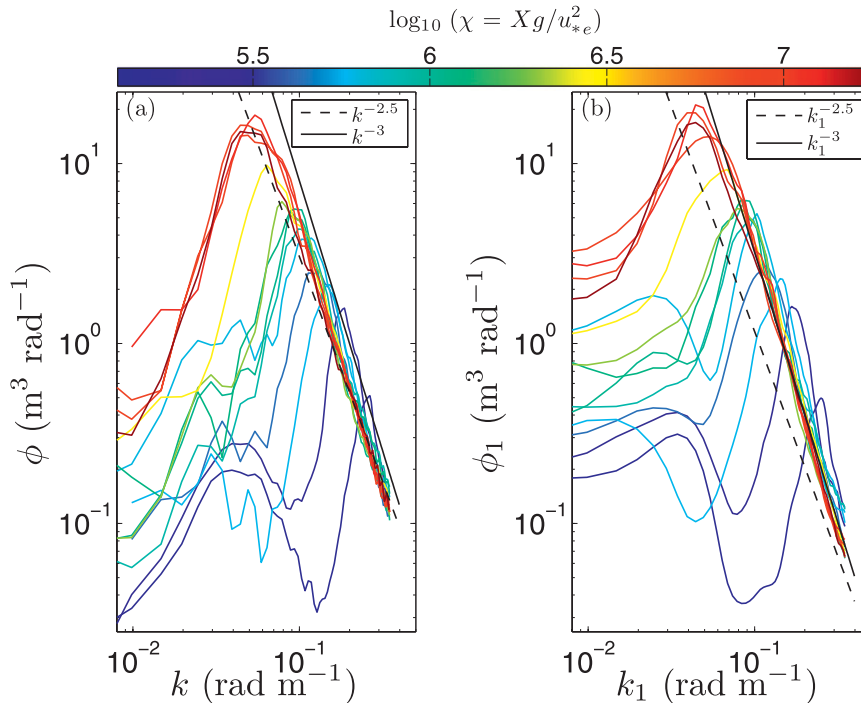


FIG. 8. Logarithmic plots of (a) omnidirectional and (b)  $k_1$  spectra from sea surface topography measurements collected during RF 05 on 17 Feb 2004. The dashed and solid black lines are reference spectral slopes proportional to  $k^{-5/2}$  and  $k^{-3}$ , respectively. Data are color coded according to the nondimensional fetch  $Xg/u_*e^2$ .

of approximately 70, 250, and 500 km. Figures 11a–c show  $k_1$  and  $k_2$  spectra from Riegl measurements, along with neighboring ATM  $k_1$  spectra. The ATM  $k_1$  spectra blend well with the Riegl spectra, showing a consistent power law of  $k_1^{-3}$  for a wide range of wavenumbers ( $2 < k_1/k_p < 40$ ). At intermediate wavenumbers, the Riegl  $k_2$  spectra show a power law of approximately  $k_2^{-5/2}$ , followed by a transition to  $k_2^{-3}$  at higher wavenumbers. In this high-wavenumber region,  $\phi_2$  approximately merges with  $\phi_1$ , suggesting a loss of preferred directionality, which is consistent with an approach to isotropy and consistent with the observations by Banner et al. (1989) at higher wavenumbers where  $F(\mathbf{k})$  is approximately  $k^{-4}$ . Figure 11d shows the corresponding ATM omnidirectional spectra  $\phi$  (solid black line), as well as approximations at higher wavenumbers ( $0.65\text{--}2 \text{ rad m}^{-1}$ ) estimated using the  $k_1$  Riegl spectra under the assumption of an isotropic directional distribution with  $\phi \sim k^{-3}$  (red line). The combined Riegl and ATM spectra imply a power-law transition from the equilibrium range where  $\phi \sim k^{-5/2}$  to the saturation range at high wavenumbers with  $\phi \sim k^{-3}$ ; a corresponding power-law transition was found in broadband frequency measurements by Forristal (1981).

The  $k_1^{-3}$  power-law behavior within the tail of the  $k_1$  spectrum (see Fig. 8) is consistent with previous

observations of wavenumber spectra. Banner (1990a) compiled published measurements of the  $k_1$  spectra, including stereophotographic measurements at high wavenumbers (Banner et al. 1989) and various airborne observations, which include Barnett and Wilkerson (1967), Jackson et al. (1985a), and Schule et al. (1971). The collated data suggest that, for wind conditions in the range of 7 to 15  $\text{m s}^{-1}$ , the tail of the  $k_1$  spectrum in the direction of the wind has a single  $k_1^{-3}$  power law over a wide bandwidth, with small variations in the proportionality constant  $B_1$ , or degree of saturation. Figure 12 shows average estimates of  $B_1$ , calculated according to Eq. (34) over the interval  $2.25k_p < k < 0.35 \text{ rad m}^{-1}$  from the ATM spectra and plotted against the effective wave age  $u_*e/c_p$ , where  $c_p$  is the linear phase speed at the spectral peak. The solid black line shows the best-fit estimate of  $B_1$  given in Eq. (50);  $B_1$  decreases with increasing wave age, varying between  $3.7 \times 10^{-3}$  for young waves and  $2.5 \times 10^3$  near full development, in qualitative agreement with the saturation values reported by Schule et al. (1971) of  $3 \times 10^{-3}$  and Barnett and Wilkerson (1967) of  $4 \times 10^{-3}$ .

At higher wavenumbers, the one-dimensional saturation for the  $k_1$  and  $k_2$  spectra  $B_i$  ( $i = 1, 2$ ) were calculated from Riegl measurements within a range of wavenumbers according to

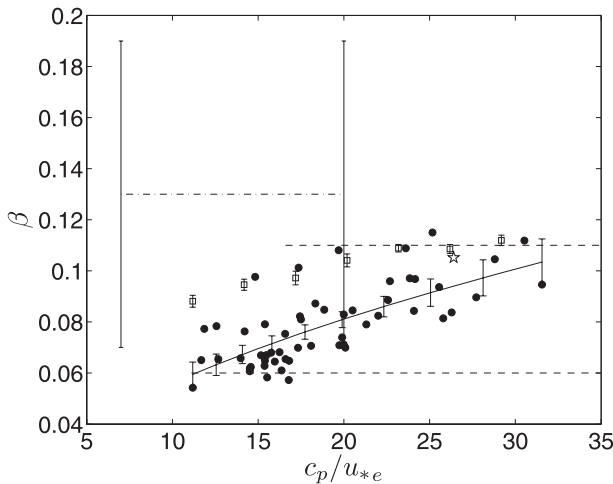


FIG. 9. Toba's parameter  $\beta$  vs the effective wave age  $c_p/u_{*e}$ . The solid circles correspond to the ATM measurements. The solid line is the best-fit estimate with 95% confidence intervals. The open star corresponds to the ATM measurements by Hwang et al. (2000a) for quasi-steady conditions. The dashed lines indicate the range of values from historical data summarized by Phillips (1985). The open squares are bin-averaged estimates obtained using the equilibrium range measurements by Resio et al. (2004) and this study's measurements of  $u_*$  and  $c_p$ . The error bars correspond to  $\pm$  one standard deviation. The dashed-dotted line with bars corresponds to the mean and standard deviation from the reanalysis of the JONSWAP data by Battjes et al. (1987).

$$B_i = \frac{1}{(k_u - k_l)} \int_{k_l}^{k_u} \phi_i(k_i) k_i^3 dk_i, \quad (i = 1, 2), \quad (34)$$

where  $k_l$  and  $k_u$  correspond to the lower and upper limits of integration, respectively. From visual examinations of the spectra, it was found that, within the range of 0.75–2  $\text{rad m}^{-1}$ , both  $\phi_2(k_2)$  and  $\phi_1(k_1)$  approximately follow a  $k^{-3}$  power-law behavior without being affected by the noise floor. Figure 13a shows  $B_1$  and  $B_2$  against the nondimensional average wavenumber  $u_*^2 k_a g$ , which is the reciprocal of the average local wave age squared, where  $k_a = 1.375 \text{ rad m}^{-1}$  corresponds to the mean value of the averaging interval (0.75–2  $\text{rad m}^{-1}$ ). The data show that within this range the saturation is approximately constant with no dependence on the local wave age, with  $B_1 = 3.2 \pm 0.9 \times 10^{-3}$  being lower than  $B_2 = (4.1 \pm 1.0) \times 10^{-3}$  by 22%, which is in excellent agreement with Melville and Matusov (2002)<sup>1</sup>, whose mean saturation values when computed over the same range of wavenumbers corresponds to  $3.2 \times 10^{-3}$ . The dotted line shows the measurements by Banner et al. (1989) at higher wavenumbers ( $1.25 < k < 10 \text{ rad m}^{-1}$ ),

<sup>1</sup> Note that the one-dimensional spectra reported in Melville and Matusov (2002) had a processing error of a factor of 2. The saturation value given has been corrected.

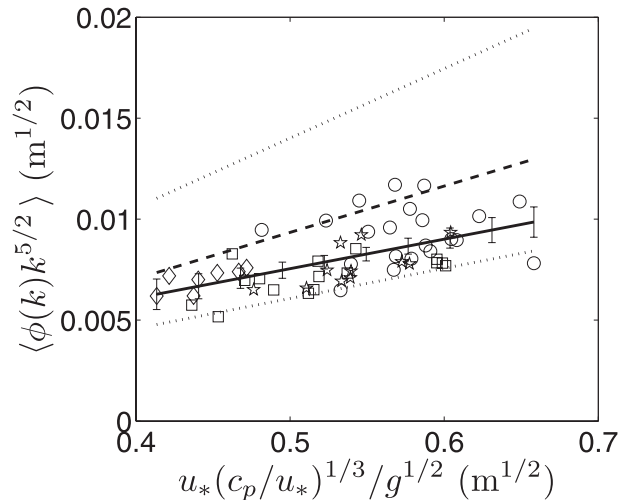


FIG. 10. Mean compensated spectra  $\langle \phi k^{5/2} \rangle$  within the equilibrium range plotted against the scaling proposed by Resio et al. (2004)  $u_*(c_p/u_*)^{1/3}/g^{1/2}$ , where  $u_*$  is friction velocity,  $c_p$  is dominant wave velocity, and  $g$  is gravity. The solid black line is the best-fit estimate with 95% confidence intervals. The dashed line is the best-fit estimate by Resio et al. (2004), and the dotted lines approximately show their range of values observed.

which show slightly larger saturation values when compared to our measurements. The overall mean saturation for both the  $k_1$  and  $k_2$  spectra combined gives  $\bar{B} = 4 \pm 1 \times 10^{-3}$ . The uncertainties of  $B_1$ ,  $B_2$ , and  $\bar{B}$  correspond to two standard deviations. By spatially interpolating  $k_p$  from the ATM omnidirectional spectra to the Riegl sampling locations, it is found that, within the saturation range, although  $B_1$  is nearly constant,  $B_2$  increases with increasing wave effective wave age, as shown in Fig. 13b. The best-fit estimate, with 95% uncertainty, yields  $B_2 = (5.9 c_p/u_{*e} + 296 \pm 28) \times 10^{-5}$ .

By assuming an isotropic directional distribution within the saturation range with  $F(k, \theta) \propto k^{-4}$  with  $-\pi/2 < \theta < \pi/2$  (Phillips 1958), the azimuth-integrated spectrum becomes

$$\phi(k) = Bk^{-3}, \quad (35)$$

where the azimuth-integrated saturation  $B = 2\bar{B}$  (Phillips 1977). Following Hwang and Wang (2001), Eqs. (35) and (31) are solved for the wavenumber component  $k_o$ , which separates the equilibrium and saturation ranges and is given by

$$k_o = \left( \frac{2B}{\beta} \right)^2 \frac{g}{u_*^2}. \quad (36)$$

Figure 14 shows  $k_o/k_p$  versus the effective wave age as estimated from Eq. (36), with  $k_o/k_p$  increasing from approximately 10 for young seas to about 23 at full development. The data showed by Long and Resio (2007)

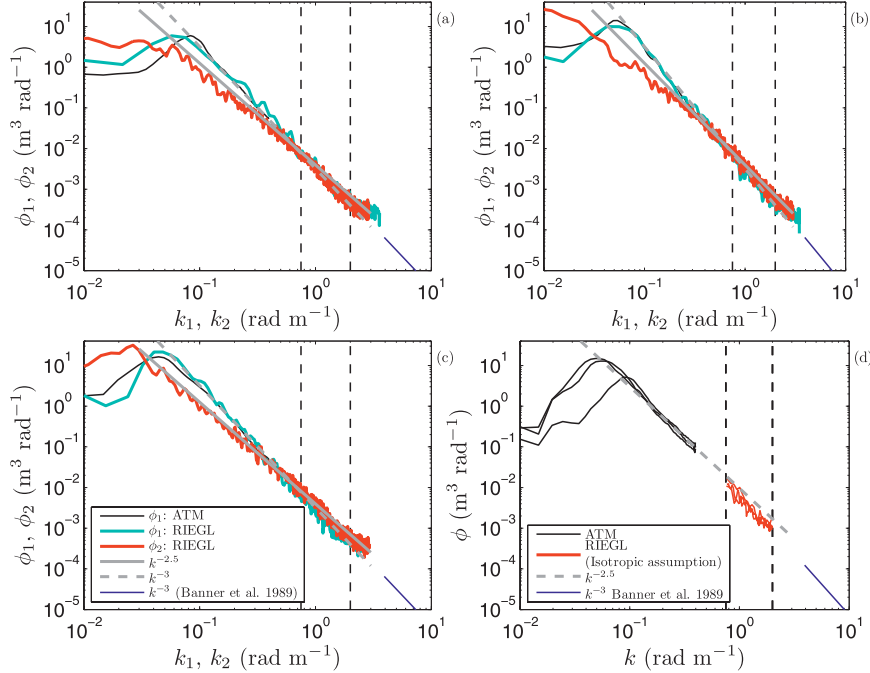


FIG. 11. Comparison of one-dimensional wavenumber spectra from measurements collected with the ATM and Riegl during RF 05. (a)–(c) One-dimensional  $k_1$  and  $k_2$  spectra,  $\phi_1$  and  $\phi_2$ , from Riegl and ATM measurements at fetches of approximately 70, 250, and 500 km, respectively. (d) The corresponding omnidirectional spectra  $\phi$  from the ATM measurements at the three fetches (solid black), and estimates at high wavenumbers ( $0.75\text{--}2 \text{ rad m}^{-1}$ ) obtained from  $k_1$  Riegl spectra assuming an isotropic directional spectrum  $F(\mathbf{k}) \propto k^{-4}$  (red). Reference slopes proportional to  $k^{-5/2}$  and  $k^{-3}$  are shown as solid and dashed gray lines, respectively. The measurements by Banner et al. (1989), at high wavenumbers, are shown in blue. The black dashed vertical lines show the averaging interval for  $B_i$  between 0.75 and  $2 \text{ rad m}^{-1}$ .

shares a similar trend in the changes of the frequency where the spectrum changes power law with respect to the wave age.

Forristal (1981) reported a transitional frequency component  $f_o$  separating the analogous power-law transition in frequency spectra, which was exclusively related to  $u_*$ . The solid gray line in Fig. 14 corresponds to Forristal’s results using our measurements of  $k_p$  and  $u_{*e}$ , assuming the linear dispersion relationship and  $u_{*e} = u_*$ . Forristal’s results underpredict our estimates of  $k_o/k_p$  for young waves and show qualitative agreement near full development. The solid black line was obtained from the best fit of  $\beta(c_p/u_{*e})$  in Eqs. (33) and (36).

To quantify the transitional wavenumber component of power law from the measured Riegl  $k_2$  spectra, we parameterize  $\phi_2(k_2)$  according to

$$\phi_2(k_2) = \alpha_2 k_2^{-5/2}, \quad (37)$$

with  $\alpha_2$  calculated as follows:

$$\alpha_2 = \frac{1}{(0.75 - 2.25k_p)} \int_{2.25k_p}^{0.75} \phi_2(k_2) k_2^{5/2} dk_2, \quad (38)$$

where  $k_p$  corresponds to the peak wavenumber of the ATM omnidirectional spectra, which was spatially interpolated to the Riegl sampling locations. Then, by matching Eq. (37) with the saturation spectrum  $\phi_2 = B_2 k_2^{-3}$  at higher wavenumbers [Eq. (34)] and solving for the transitional wavenumber component  $k_{2o}$ , it is found that  $k_{2o}/k_p$  also increases with increasing wave age (see Fig. 14). However,  $k_{2o}$  is larger than  $k_o$ , on average.

### c. Other moments of the spectrum

Field observations and numerical investigations have shown that the directional wind-wave spectrum is narrowest near the peak and broader toward both lower and higher wavenumbers (Hasselmann et al. 1980; Banner and Young 1994; Hwang et al. 2000b). The directional spreading  $\sigma_\theta$  of a symmetric wind-wave spectrum can be estimated from the first moment over one side of the spectrum (Banner and Young 1994). However, in a situation with turning winds, as in the Gulf of Tehuantepec, the directional spectra may not be symmetric (see, e.g., Long and Resio 2007). More generally, the directional spreading can be estimated as the

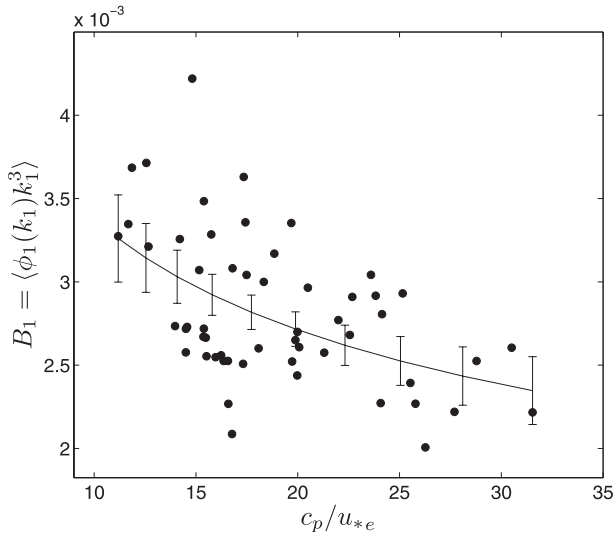


FIG. 12. Degree of saturation within the tail of the ATM  $k_1$  spectra vs the effective wave age. The solid line is the best-fit estimate with the 95% confidence intervals.

average spreading from both sides of the spectrum according to

$$\sigma_\theta(k) = \frac{\int_{-\pi/2}^{\pi/2} F(k, \theta) |\theta| d\theta}{\int_{-\pi/2}^{\pi/2} F(k, \theta) d\theta}. \quad (39)$$

Figure 15a shows the observed directional spreading defined by Eq. (39), with each profile corresponding to a bin average of 9–10 spectra according to the range of wave ages shown. The error bars shown correspond to the bin-averaged directional resolution  $\langle d\theta \rangle$ . The spreading  $\sigma_\theta(k)$  shows a weak dependence (indistinguishable within error bars) on the wave age, with younger waves having a spectrum narrower near the peak and broader for  $k/k_p > 2$ . The measured directional spreading, or spectral width in the azimuthal direction, is qualitatively in agreement with the observations by Hwang et al. (2000b) for a quasi-steady wave field. The observed spectra of younger waves, with good directional resolution near the spectral peak, show that the spectrum is narrowest slightly below  $k_p$ , in agreement with the measurements by Babanin and Soloviev (1998).

All previous studies of wind waves have focused on the directional spreading in the azimuthal direction. In this study, we present another measure, the spreading in the  $k_2$  direction as a function of  $k_1$  (the component along the dominant wave direction) defined by

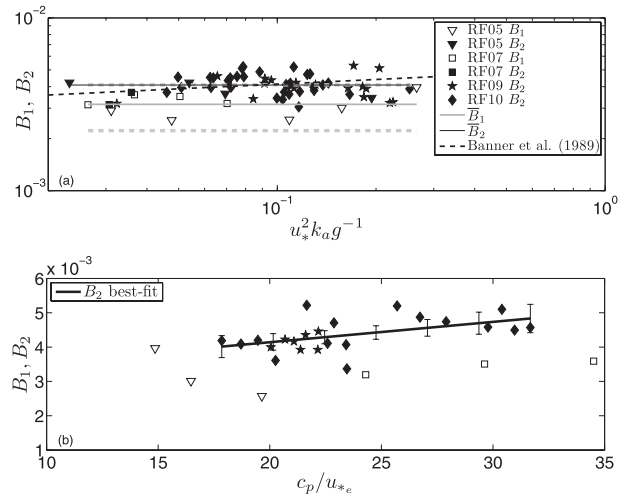


FIG. 13. One-dimensional saturation values,  $B_1$  and  $B_2$ , estimated according to Eq. (34) from Riegl measurements at high wavenumbers, between 0.75 and 2  $\text{rad m}^{-1}$ . (a) The saturation is plotted vs the nondimensional mean wavenumber component,  $u_{*e}^2 k_a g^{-1}$ , where  $k_a = 1.375 \text{ rad m}^{-1}$ . (b) The saturation is shown vs the effective wave age. The solid black line corresponds to the best fit with 95% confidence intervals. The spectral peak wavenumber was spatially interpolated at the Riegl sampling locations from the available ATM observations.

$$\sigma_2(k_1) = \frac{\left[ \int_{-k_{2n}}^{k_{2n}} F(k_1, k_2) k_2^2 dk_2 \right]^{1/2}}{\left[ \int_{-k_{2n}}^{k_{2n}} F(k_1, k_2) dk_2 \right]}, \quad (40)$$

where  $k_{2n} = 0.5 \text{ rad m}^{-1}$ . When  $\sigma_2$  is normalized by the peak wavenumber  $k_p$  and plotted against  $k_1/k_p$ , the data collapse onto a single curve independent of wave age, as shown in Fig. 15b. This highlights the approximate self-similar nature of the fetch-limited wave field and suggests the possibility of a simple parameterization of the directional distribution in the  $(k_1, k_2)$  plane.

Socquet-Juglard et al. (2005) used the second moment of the spectrum in the  $k_2$  direction integrated over all  $k_1$  wavenumbers to define the mean crest length as

$$\bar{\Lambda}_c = 2\pi \left[ \frac{\int \int F(k_1, k_2) k_2^2 dk_1 dk_2}{\int \int F(k_1, k_2) dk_1 dk_2} \right]^{-1/2}. \quad (41)$$

Similarly, from Eq. (40), the mean spectral crest length  $\Lambda_c(k_1)$  with carrier wavenumber  $k_1$  can be defined as

$$\Lambda_c(k_1) = \frac{2\pi}{\sigma_2(k_1)}. \quad (42)$$

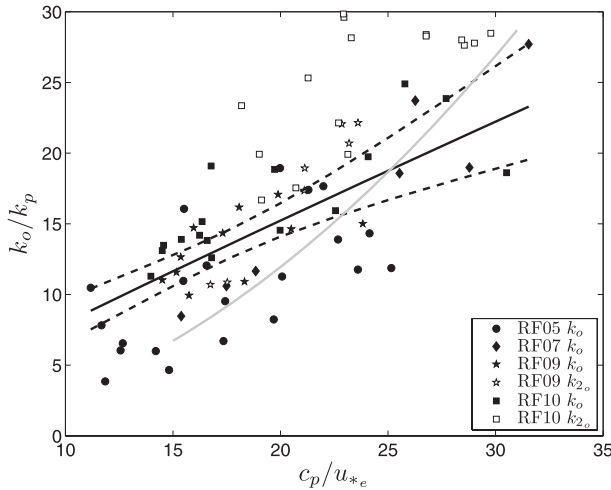


FIG. 14. Transition wavenumber  $k_o/k_p$  between the  $k^{-5/2}$  and  $k^{-3}$  power-law behaviors for the omnidirectional and  $k_2$  spectra, plotted vs  $c_p/u_{*e}$ . The solid black line corresponds to Eq. (36) with the best-fit estimates of  $\beta$  in Eq. (33). The dashed lines show the 95% confidence interval. The gray line corresponds to the parameterization by Forristal (1981) using our measurements of  $k_p$  and  $u_{*e}$ , assuming  $u_* = u_{*e}$ .

Thus, Fig. 15b suggests that, within the range  $1 < k/k_p < 5$ ,  $\Lambda_c$  is linearly related to the carrier wavelength ( $\lambda_1 = 2\pi/k_1$ ). The expression  $\sigma_2(k_1)/k_p$  yields a linear regression of

$$\frac{\sigma_2(k_1)}{k_p} = 0.81 \frac{k_1}{k_p} - 0.25. \quad (43)$$

d. Bimodal structure

Early observations of directional frequency spectra, such as Mitsuyasu et al. (1975) and Hasselmann et al. (1980), reported azimuthal spreading functions with unimodal distributions for all frequencies. In contrast, all previous airborne spatial wave measurements (Cote et al. 1960; Holthuijsen 1983; Jackson et al. 1985b; Wyatt 1995; Hwang et al. 2000a,b) have found bimodal directional distributions for wavenumbers larger than the spectral peak. Recently, bimodal structures have also been extracted from spatiotemporal (Long and Resio 2007) and buoy observations (Young et al. 1995; Ewans 1998; Wang and Hwang 2001; Long and Resio 2007), but the buoy results are strongly dependent on the method used to process the data (Benoit 1992; Krogstad 1990). Numerical studies by Banner and Young (1994), Dysthe et al. (2003), and Pushkarev et al. (2003) suggest that the bimodal distribution developed in computed spectra, for frequencies both lower and higher than the spectral peak, is a robust feature of the wave spectrum resulting from the nonlinear resonant interactions.

Figure 16 shows the typical directional wavenumber spectra in Cartesian (Fig. 16a) and polar (Fig. 16b) rep-

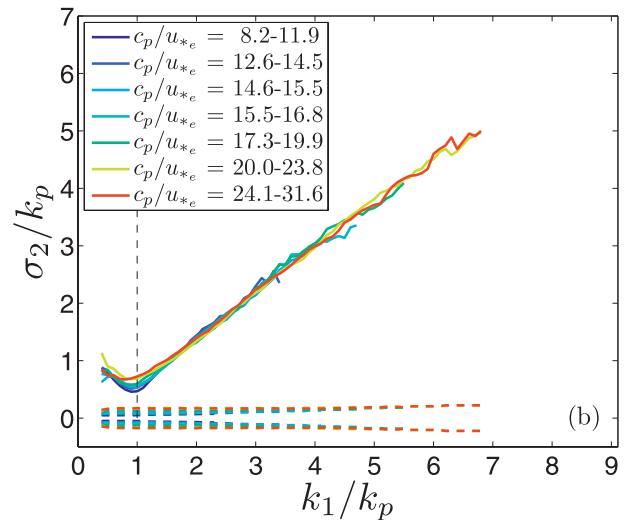
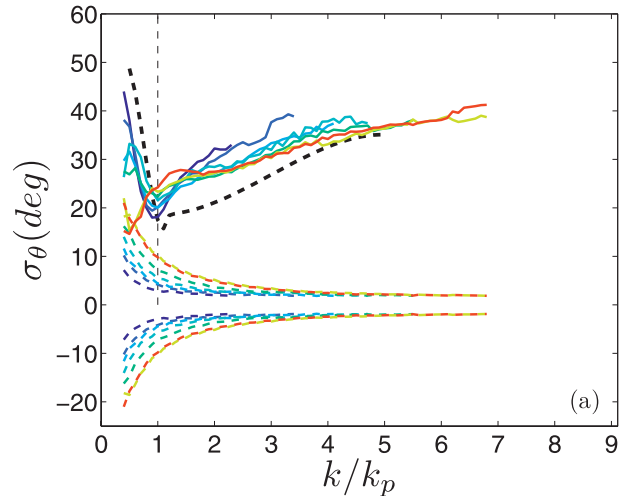


FIG. 15. (a) Directional spreading and (b) spectral width along the axis  $k_2$  orthogonal to the dominant waves ( $k_1$ ) calculated from Eqs. (39) and (40). The curves shown correspond to bin averages of 9–10 spectra for the range of wave ages ( $c_p/u_{*e}$ ) shown. The dashed lines show the bin-averaged resolution. The directional spreading by Hwang et al. (2000b) for quasi-steady conditions is shown with a black dashed line.

resentations. Figure 16c shows the normalized spectrum  $F(k, \theta)/F(k, 0)$ , where  $\theta = 0$  corresponds to the dominant wave direction, for  $k/k_p = 1, 2, 3, 4$ . Near the spectral peak, the directional distribution is unimodal, but it becomes bimodal at higher wavenumbers. Following Wang and Hwang (2001), the bimodal structure at high wavenumbers can be characterized with two parameters, the azimuthal separation between the lobes  $\theta_{lobe}$  and the average amplitude of the lobes relative to the spectral energy in the dominant wave direction  $r_{lobe}(k)$ :

$$\theta_{lobe}(k) = \frac{|\theta_1(k)| + |\theta_2(k)|}{2} \quad \text{and} \quad (44)$$

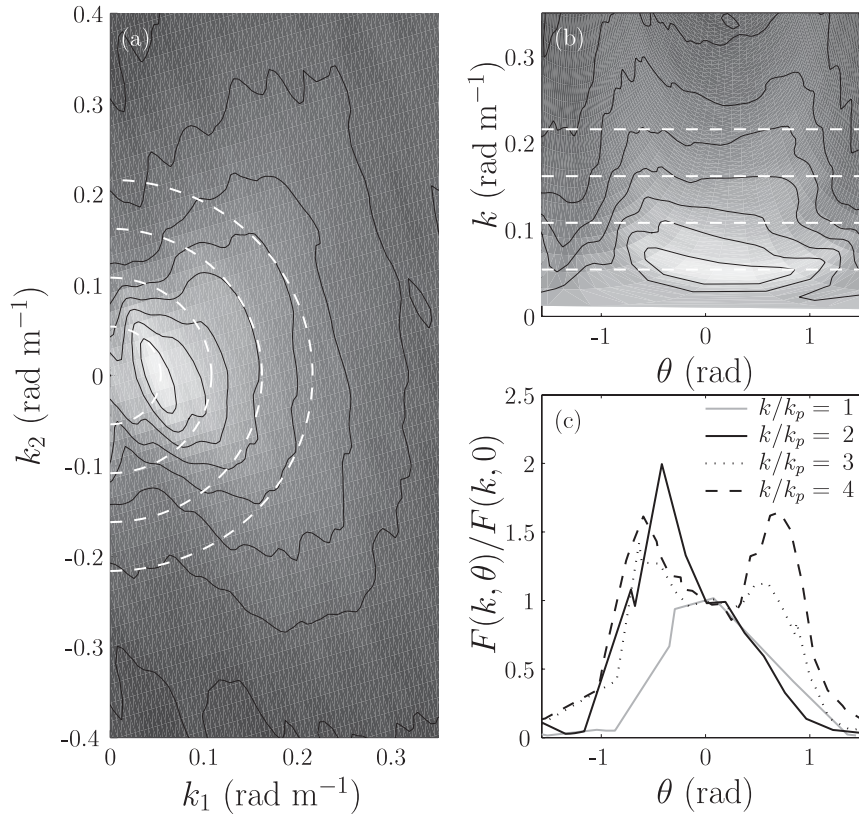


FIG. 16. Sample directional wavenumber spectra corresponding to RF 05 from ATM measurements collected at a fetch of 200 km. (a) The spectrum is shown in Cartesian representation  $F(k_1, k_2)$ , and (b) it is plotted in polar representation  $F(k, \theta)$ . (c) The normalized spectrum in polar coordinates at wavenumbers  $k/k_p = 1, 2, 3,$  and  $4$ . The white dashed lines show constant  $k$ .

$$r_{\text{lobe}}(k) = \frac{1}{2} \frac{F(k, \theta_1) + F(k, \theta_2)}{F(k, 0)}, \quad (45)$$

where  $\theta_1(k)$  and  $\theta_2(k)$  are the azimuthal location of the maxima at a given wavenumber on each side of the spectrum relative to the dominant wave direction.

The buoy observations of Wang and Hwang (2001) suggest that the bimodal distribution is invariant with wave age. This contrasts with the buoy measurements by Ewans (1998) in conjunction with the results from a wave gauge array by Long and Resio (2007), which suggest that the bimodal separation of the spectrum is weakly dependent on the wave age. The extensive dataset of wavenumber spectra from GOTEX, covering a wide range of wave ages, permits the investigation of the dependence of the bimodal structure on the wave age.

Figures 17a,b show bin averages of  $\theta_{\text{lobe}}(k/k_p)$  and  $r_{\text{lobe}}(k/k_p)$  from 9 to 10 spectra, over the range of wave ages shown in Fig. 15b, with error bars corresponding to bin averages of the directional resolution and the uncertainty at the 95% confidence interval (see section 3b), respectively. Here,  $\theta_{\text{lobe}}$  shows a weak dependence on

the wave age, with younger waves having a larger lobe separation, which is qualitatively consistent with Ewans (1998), and  $r_{\text{lobe}}$  also shows a dependence on wave age, differing from the observations of Wang and Hwang (2001). The values of  $\theta_{\text{lobe}}$  and  $r_{\text{lobe}}$  for mature waves reported by Hwang et al. (2000b; open circles) show qualitative agreement with this study. Also shown (solid gray line) are the measurements of  $\theta_{\text{lobe}}$  by Long and Resio (2007) for young waves, with an inverse wave age of  $1.6 < U_{10}/c_p < 3.4$  corresponding to  $7 < c_p/u_{*e} < 16$ , assuming a drag coefficient of  $1.5 \times 10^{-3}$ . Finally, the black diamonds are from a GOTEX spectrum measured while flying crosswind, near shore, where  $c_p/u_{*e}$  was approximately 12. The bimodal structure given by the spectrum from the crosswind leg shows qualitatively the same behavior as the downwind spectra; thus, the bimodal distribution is independent of the flight orientation relative to the waves.

When  $\theta_{\text{lobe}}$  and  $r_{\text{lobe}}$  are multiplied by  $0.2 \times (c_p/u_{*e})^{1/2}$ , both sets of curves collapse reasonably well, see Figs. 17c,d. Second-order polynomial fits, for  $1.5 < k/k_p < 6.5$ , yield

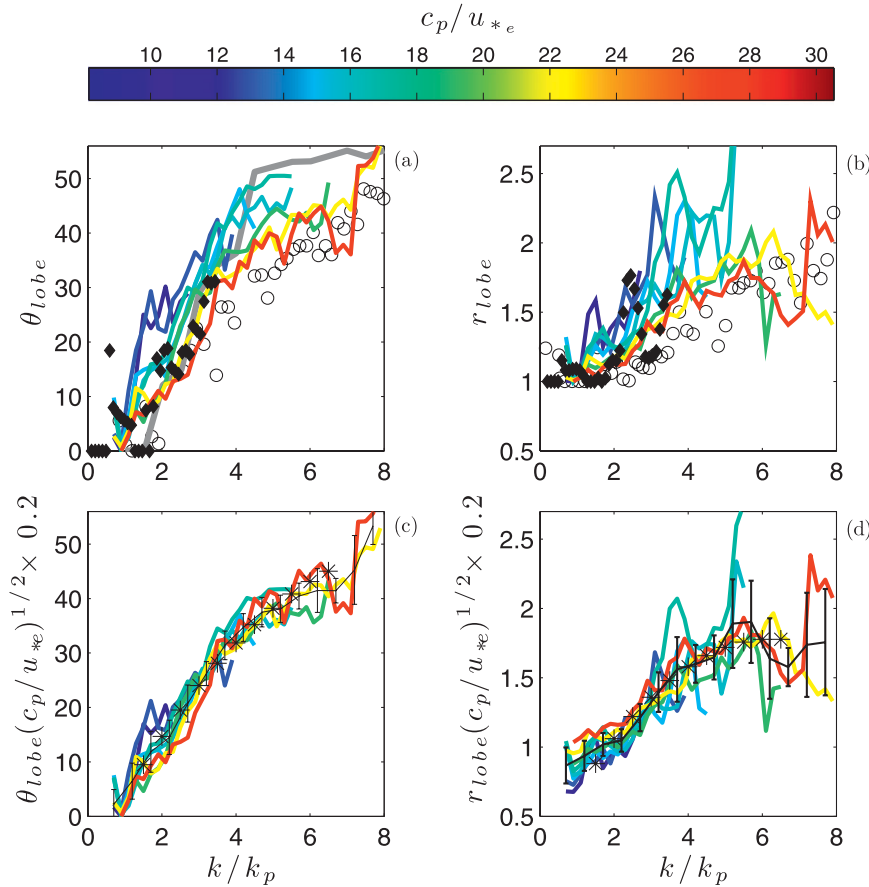


FIG. 17. Bin-averaged (a) lobe separation  $\theta_{lobe}(k/k_p)$  and (b) relative amplitude  $r_{lobe}(k/k_p)$  over the range of wave ages shown. The curves shown correspond to bin averages of 9–10 spectra. The open circles correspond to the measurements by Hwang et al. (2000b). The solid gray line shows the field measurements by Long and Resio (2007). The black diamonds correspond to a sample spectrum obtained from a crosswind track during RF 05, where the effective wave age  $c_p/u_{*e} = 12$ . The terms (c)  $\theta'_{lobe}$  and (d)  $r'_{lobe}$  are scaled with  $(c/u_{*e})^{1/2}$ . The solid black line is a bin average with error bars of one standard deviation. The black asterisks are the polynomial best fits from Eqs. (46) and (47).

$$\theta'_{lobe} = -0.736 \left( \frac{c_p}{u_{*e}} \right)^2 + 12.9 \left( \frac{c_p}{u_{*e}} \right) - 8.35 \quad \text{and} \quad (46)$$

$$r'_{lobe} = -0.04 \left( \frac{c_p}{u_{*e}} \right)^2 + 4.9 \left( \frac{c_p}{u_{*e}} \right) + 0.22, \quad (47)$$

where  $\theta'_{lobe} = 0.2(c_p/u_{*e})^{1/2} \theta_{lobe}$  and  $r'_{lobe} = 0.2(c_p/u_{*e})^{1/2} r_{lobe}$ .

**5. Wavenumber spectrum parameterization**

In this section, the observed self-similar features of the wind-wave spectra are used to construct a parameterization of the  $k_1$  spectrum with dependence on the dimensionless fetch or wave age. Figure 18a shows the

typical compensated  $k_1$  spectra,  $\phi k_1^3$ , versus  $k_1/k_p$ , suggesting that  $\phi_1$  can be approximated by a double power-law model, with a spectral tail  $\propto k_1^{-3}$  and the forward face  $\propto k_1^4$ , with a peak enhancement function between the two. Based on the JONSWAP peak enhancement function (Hasselmann et al. 1973), the following spectral parameterization is proposed:

$$\phi_1(k_1, X, u_{*e}, g) = \frac{B_1 \gamma^{\exp\{-[1-(k_1/k_p)^2]^2/2\sigma^2\}}}{k_1^3 + k_p^3 \left( \frac{k_1}{k_p} \right)^{-4}}, \quad (48)$$

where  $B_1$ ,  $\sigma$ , and  $\gamma$  are empirical parameters that may depend on the dimensionless fetch or the wave age;  $B_1$  is the degree of saturation in the  $k_1$  direction, and  $\gamma$  and

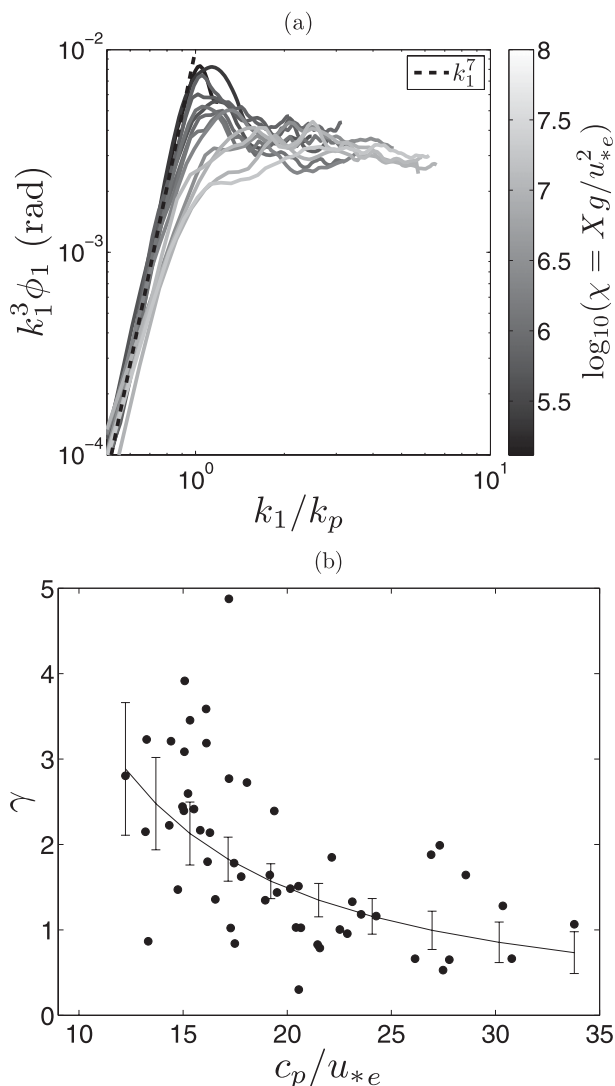


FIG. 18. (a) Typical compensated  $k_1$  spectra times  $k_1^3$  vs  $k_1/k_p$  for RF 05 at various nondimensional fetches  $Xg/u_{*e}^2$ , ranging from  $10^5$  to  $10^7$ . The dashed black line is a reference slope  $\propto k_1^7$ . (b) The  $k_1$  spectrum peakedness factor  $\gamma$  vs the effective wave age. The solid line corresponds to the best fit with 95% confidence intervals.

$\sigma$  represent the amplitude and width of the peak enhancement, respectively. Figures 12 and 18b show the estimates  $B_1$  and  $\gamma$  versus the effective wave age; both parameters decrease with increasing  $c_p/u_{*e}$  according to following relations:

$$B_1 = 7.01 \times 10^3 \left( \frac{c_p}{u_{*e}} \right)^{-3.2 \pm 0.2 \times 10^{-1}} \quad \text{and} \quad (49)$$

$$\gamma = 8.43 \times 10^1 \left( \frac{c_p}{u_{*e}} \right)^{-1.35 \pm 0.06}, \quad (50)$$

with uncertainties corresponding to the 95% confidence intervals. The fit to the peakedness factor reaches unity at about  $c_p/u_{*e} = 28$  and continues to decrease at the larger wave ages, giving rise to a peak reduction. Of the other parameters,  $\sigma$  was kept constant with a value of 0.5,  $B_1$  was estimated as described in section 4b, and  $\gamma$  was fitted using Newton's iterative method. The spectral peakedness reduction with increasing wave age is consistent with the results by Mitsuyasu (1981), Donelan et al. (1985), and Long and Resio (2007) for frequency spectra. Figure 19 shows a direct comparison between observed  $k_1$  spectra and the parameterization using the measured values of  $k_p$  and  $u_{*e}$  as input. The parameterization of the spectrum can reproduce the measurements fairly well (within the uncertainty at the 95% confidence interval) at young to intermediate wave ages. Toward full development, at very large fetches, the model cannot reproduce the measurements below the spectral peak, because the forward face of the measured spectrum falls off less steeply than the  $k_1^4$  slope. This may be attributed to the reduced spectral resolution at low wavenumbers or the presence of swell from the North Pacific, orthogonal to the local wind sea outside the Gulf of Tehuantepec.

## 6. Discussion and conclusions

The wind-wave measurements collected in the Gulf of Tehuantepec during strong offshore wind conditions are unique for having one- and two-dimensional wavenumber spectra in fetch-limited conditions covering a wide range of wave ages, from young to nearly fully developed seas. The observations are also unique for having supporting wind and turbulent flux measurements. Previous similar wind-wave studies are limited to frequency spectra and the mean winds, thus relying on parameterizations of the drag coefficient to infer the wind stress. Wind-wave measurements in the wavenumber domain are relatively rare in the literature, and those available are limited by the range of environmental conditions. However, wavenumber wind-wave observations are preferred over frequency spectra, which can be distorted at high frequencies because of the Doppler shift induced by the steeper and longer dominant waves (Kitaigorodskii et al. 1975; Banner 1990a).

Although the GOTEX measurements were collected under spatially inhomogeneous and veering winds, the data conform with the well-established fetch relations from previous observations when appropriate definitions of the friction velocity and fetch are used. In particular, we find good agreement with the reanalysis by Kahma and Calkoen (1992) for waves generated during a stably stratified atmospheric boundary layer. Most of our measurements at short to intermediate fetches were

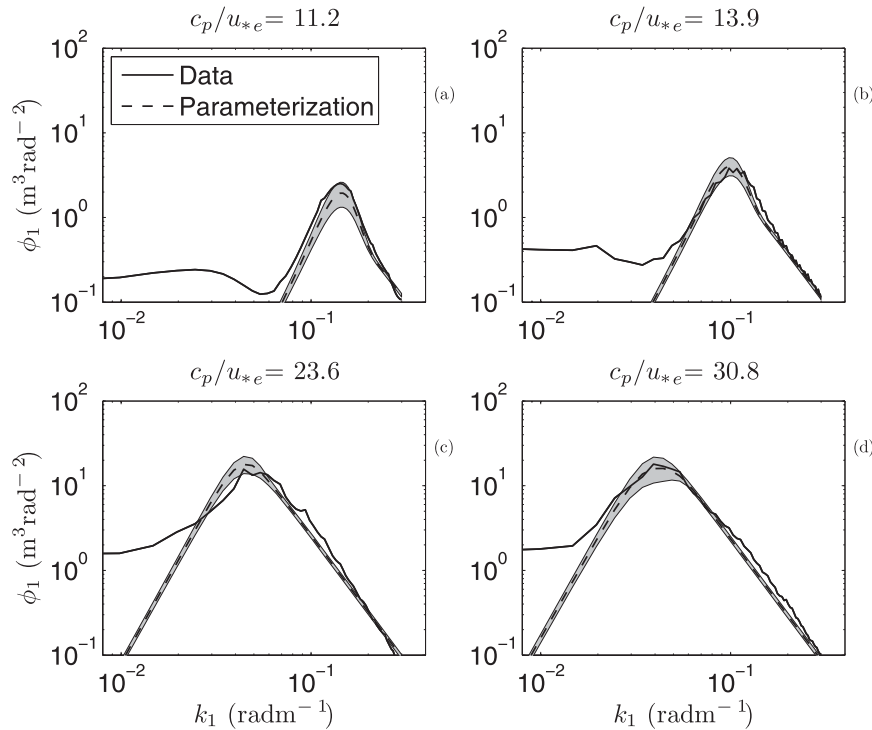


FIG. 19. Comparison between measured (solid lines) and parameterized  $k_1$  spectra (dashed lines) for  $c_p/u_{*e}$  values of 11.2, 13.9, 23.6, and 30.8. The gray shaded area represents the 95% confidence intervals.

collected in stable atmospheric conditions because of the strong upwelling and entrainment induced by the strong offshore wind forcing bringing cooler water to the surface. In the context of wind-wave modeling, this suggests that to leading order the integral effects resulting from spatial changes in the wind field in GOTEX must be small compared to the net forcing, which includes the wind forcing, nonlinear energy flux resulting from resonant interactions, and dissipation resulting from wave breaking. This is consistent with the numerical experiments by Young et al. (1987), where it was shown that, for sudden changes in the wind direction of less than  $60^\circ$ , the entire spectrum rotated into the new wind direction, with high-frequency components adjusting faster than the low frequencies. Although the wind input forced the spectrum in the new wind direction, the dissipation damped out the components in the old wind direction and the nonlinear transfer ensured a smooth rotation, preventing the appearance of the secondary peaks.

The measured wavenumber spectra exhibit self-similar properties with a weak but significant dependence on the effective wave age. The omnidirectional spectrum, within the equilibrium range, follows a power law approximately proportional to  $k^{-5/2}$ . Following Toba's scaling,  $\beta$  is not constant, showing an increasing trend with increasing effective wave age. This is qualitatively consistent with

frequency measurements by Resio et al. (2004). However, there is a clear discrepancy in the overall magnitude of  $\beta$  among the various observations. This could be attributed to differences in atmospheric stability, which are known to affect the observed growth rate of the wave field (see, e.g., Kahma and Calhoun 1992; Young 1998). However it is not clear from the available measurements in the literature how  $\beta$  changes with respect to atmospheric stability. The GOTEX measurements, with lower values of  $\beta$ , were collected mainly under a stably stratified boundary layer and are in good agreement with the wave measurements by Hwang et al. (2000a) under weakly unstable air-sea conditions. Although not explicitly addressed in their text, the measurements of Resio et al. (2004) must include data in both stable and unstable regimes, because they were collected in various locations around the world. Figure 10 shows our measurements using the scaling of the equilibrium range by Resio et al. (2004), with the GOTEX measurements within the range of values reported by them. However, there is a poor correlation between the observed variability of  $\beta$  and the stability parameter  $z_r/L$ . Other external factors that may affect the observed values of  $\beta$  include modulations resulting from the presence of varying surface currents and the stationarity assumption of the wind field inherent in the analysis.

Although the one-dimensional  $k_1$  spectra show a consistent power law proportional to  $k_1^{-3}$  over a wide range of wavenumbers, the  $k_2$  spectra are better described by two power laws:  $k_2^{-5/2}$  at low wavenumbers and  $k_2^{-3}$  at high wavenumbers. In the region immediately after the peak, the one-dimensional  $k_1$  saturation  $B_1$  decreases with increasing effective wave age. However, at high wavenumbers within the saturation range,  $B_1$  and  $B_2$  are almost independent of the local  $u_*$ , with  $B_2 = 4.1 \times 10^{-3}$  and  $B_1 = 3.2 \times 10^{-3}$ . The comparison of the Riegl one-dimensional  $k_1$  and  $k_2$  spectra (Fig. 11) indicates that, at intermediate wavenumbers, where  $\phi_1 > \phi_2$ , the directional spectra must be clearly anisotropic, which is also supported by the measured ATM directional spectra. However, at higher wavenumbers, the Riegl measurements show that  $\phi_1 \approx \phi_2$ , which is consistent with an approach toward isotropy.

By assuming an isotropic directional distribution for the saturation range, the omnidirectional saturation  $B$  becomes  $2\bar{B}$  (Phillips 1977, p. 150), which is 30% lower than the saturation values reported by Forristal (1981), based on a large dataset of frequency spectra over a similar range of forcing conditions, and is in close agreement with the mean values reported by Banner et al. (1989). Extrapolation of the equilibrium spectrum to match the constant saturation region gives a transition wavenumber  $k_o$ , which separates the equilibrium and saturation ranges. Here,  $k_o/k_p$  increases with wave age, ranging between 10 and 23, differing from the results by Forristal (1981) that give a transition exclusively dependent on the local forcing. The discrepancy between Forristal's and this study's estimates of  $k_o/k_p$  is reasonable, given the possible distortions of frequency spectra resulting from Doppler shifting at large frequencies. Phillips (1985) suggests that the use of the linear dispersion relation for the mapping of the spectrum from wavenumber to frequency space may be limited to a range of frequencies where the intrinsic phase speed is much greater than the orbital velocity of the dominant waves, which is proportional to  $2\langle\eta^2\rangle^{1/2}w_p$ . These results on  $k_o/k_p$  also contrast with the equilibrium range model of Hara and Belcher (2002), which predicts the power-law transition at wavenumbers as high as  $50 \text{ rad m}^{-1}$  or greater. The observed changes in power law of the Riegl  $k_2$  spectra, from  $k_2^{-5/2}$  to  $k_2^{-3}$ , were estimated to occur at the wavenumber  $k_{2o}/k_p$ , which also increases with increasing effective wave age, but  $k_{2o}$  is on average larger than  $k_o$ .

For wavenumbers greater than twice the peak wavenumber ( $k/k_p > 2$ ), the normalized width of the spectrum in the direction orthogonal to the wind is approximately independent of the wave age and increases with increasing wave age near the spectral peak ( $0.5 < k/k_p < 1.5$ ). In

contrast, the directional spreading, or spectral width in the azimuthal direction, for  $k/k_p > 2$ , decreases with increasing wave age. Similarly, within the bimodal structure of the spectrum, both the amplitude and separation of the lobes show a reduction with increasing wave age at a rate proportional to  $(c_p/u_{*e})^{1/2}$ . The observed dependence of  $\theta_{\text{lobe}}$  on the wave age is more or less consistent with that suggested by Ewans (1998) and Long and Resio (2007); however, to our knowledge, no previous work has found a clear relationship between  $r_{\text{lobe}}$  and the wave age. Finally, the self-similar features of the observed spectra were used to formulate a parameterization of the  $k_1$  spectrum with parametric dependence on the effective friction velocity and fetch.

*Acknowledgments.* We acknowledge the collaboration of Carl A. Friehe and Djamel Khelif at the University of California, Irvine, in planning and conducting the GOTEX experiments and in help with the analysis of the atmospheric boundary layer data. We are grateful to Allen Schanot, Henry Boynton, Lowell Genzlinger, Ed Ringleman, and the support staff at the NCAR Research Aviation Facility. We thank Bill Krabill, Bob Swift, Jim Yungel, John Sonntag, and Robbie Russell at NASA/EG&G for access to the ATM, its deployment, and initial data processing. We acknowledge the collaboration of Graciella Raga, Darrel Baumgardner, and students from the Universidad Nacional Autonoma de Mexico. We thank the management and staff at the Huatulco airport for their support during the field experiment. We acknowledge the assistance of Jim Lasswell and Axel Pierson at Scripps Institution of Oceanography in preparing equipment and logistical support during the field experiments. LR is grateful to Jessica Kleiss for fruitful discussion during the analysis of the data. We are thankful to Paul Hwang for useful comments and suggestions on the data analysis procedures before the field campaign and to anonymous reviewers whose comments and questions have improved the final paper. We thank Terri Paluszkiwicz, whose encouragement and support were critical in making this research possible. This research was supported by grants from the National Science Foundation (Ocean Sciences), ONR (Physical Oceanography), and BP.

## APPENDIX

### Calculation of Toba's Parameter

The tail of  $\phi(k)$  measured with the ATM is mostly proportional to  $k^{-5/2}$ , with the exception of a few cases when the spectral tail decays a little more rapidly. To

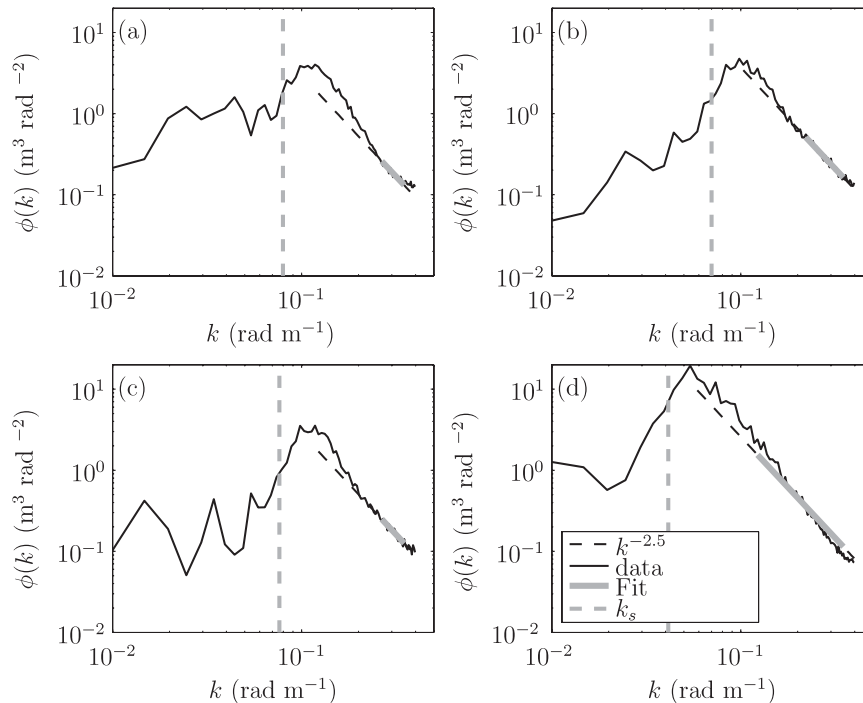


FIG. A1. Typical  $k^{-5/2}$  power-law fits within the tail of the omnidirectional spectra. The gray lines correspond to the fits to Eq. (31) within the range  $2.25k_p < k < 0.35$ , and the black dashed lines correspond to extrapolations of the fits toward both higher and lower wavenumbers. (a)–(c) Typical fits with rms errors of 15% or less and (d) a fitting case with rms error of 23%. The dashed gray line indicates the location of the wavenumber  $k_s$ , separating the wind-sea part of the spectrum from the swell.

estimate  $\beta$  from the measurements of  $\phi$ , first the mean compensated spectrum is calculated according to

$$\langle \phi(k)k^{5/2} \rangle = \frac{1}{0.35 - 2.25k_p} \int_{2.25k_p}^{0.35} \phi(k)k^{5/2} dk, \quad (\text{A1})$$

where the low wavenumber limit was set according to Donelan et al. (1985) to avoid contamination from the spectral peak and the upper limit was kept fixed at  $0.35 \text{ rad m}^{-1}$ , thus avoiding the instrumental noise. Then,  $\beta$  was calculated as

$$\beta = \frac{2g^{1/2}}{u_*} \langle \phi(k)k^{5/2} \rangle. \quad (\text{A2})$$

Because the observations close to the shore have dominant wavenumbers near the upper limit of  $0.35 \text{ rad m}^{-1}$ , the analysis of  $\beta$  was restricted to spectra with peak wavenumbers of  $0.946 \text{ rad m}^{-1}$  or smaller, corresponding to a minimum upper limit of  $2.7k_p$  in Eq. (A2). Figure A1 shows the typical azimuth-integrated spectra  $\phi(k)$ , including the fits to Eq. (31). Figures A1a–c correspond to cases where the root-mean-square error of the fit was 15% or less. Figure A1d corresponds to the

case with the largest rms error of 23%. Careful examination of the data showed that cases with an rms error larger than 15% corresponded to situations where the spectral slope of  $\phi(k)$  was steeper than  $k^{-5/2}$ . However, this only occurred for 27% of all the spectra analyzed.

REFERENCES

Alves, J. H. G. M., M. L. Banner, and I. R. Young, 2003: Revisiting the Pierson–Moskowitz asymptotic limits for fully developed wind waves. *J. Phys. Oceanogr.*, **33**, 1301–1323.

Arduin, F., T. H. C. Herbers, K. P. Watts, G. P. van Vledder, R. Jensen, and H. C. Graber, 2007: Swell and slanting-fetch effects on wind wave growth. *J. Phys. Oceanogr.*, **37**, 908–931.

Babanin, A. V., and Y. P. Soloviev, 1998: Variability of directional spectra of wind-generated waves, studied by means of wave staff arrays. *Mar. Freshwater Res.*, **49**, 89–101.

Badulin, S. I., A. N. Pushkarev, D. Resio, and V. E. Zakharov, 2005: Self-similarity of wind-driven seas. *Nonlinear Processes Geophys.*, **12**, 891–945.

Banner, M. L., 1990a: Equilibrium spectra of wind waves. *J. Phys. Oceanogr.*, **20**, 966–984.

—, 1990b: The influence of wave breaking on the surface pressure distribution in wind-wave interactions. *J. Fluid Mech.*, **211**, 463–495.

—, and W. K. Melville, 1976: On the separation of air flow over water waves. *J. Fluid Mech.*, **77**, 825–842.

- , and I. R. Young, 1994: Modeling spectral dissipation in the evolution of wind waves. Part I: Assessment of existing model performance. *J. Phys. Oceanogr.*, **24**, 1550–1570.
- , I. S. F. Jones, and J. C. Trinder, 1989: Wavenumber spectra of short gravity waves. *J. Fluid Mech.*, **198**, 321–344.
- Barnett, T. P., and J. C. Wilkerson, 1967: On the generation of ocean wind waves as inferred from airborne radar measurements of fetch-limited spectra. *J. Mar. Res.*, **25**, 292–328.
- Battjes, J. A., T. J. Zitman, and L. H. Holthuisen, 1987: A reanalysis of the spectra observed in JONSWAP. *J. Phys. Oceanogr.*, **17**, 1288–1295.
- Benoit, M., 1992: Practical comparative performance survey of methods used for estimating directional wave spectra from heave pitch roll data. *Proc. 23rd Int. Conf. on Coastal Engineering*, Vol. 2, Venice, Italy, ASCE, 162–175.
- Bidlot, J.-R., and Coauthors, 2007: Inter-comparison of operational wave forecasting systems. *Proc. 10th Int. Workshop on Wave Hindcasting and Forecasting and Coastal Hazard Symp.*, North Shore, HI, U.S. Army Engineer Research and Development Center Coastal and Hydraulics Laboratory, 1–22.
- Bretschneider, C., 1952: The generation and decay of wind waves in deep water. *Trans. Amer. Geophys. Union*, **33**, 381–389.
- Brown, E. N., C. A. Friehe, and D. H. Lenschow, 1983: The use of pressure fluctuations on the nose of an aircraft for measuring air motion. *J. Climate Appl. Meteor.*, **22**, 171–180.
- Cote, L. J., and Coauthors, 1960: The directional spectrum of a wind generated sea as determined from data obtained by the Stereo Wave Observation Project. Tech. New York University College of Engineering Rep. 6, 88 pp.
- Dobson, F., W. Perrie, and B. Toulany, 1989: On the deep water fetch laws for wind-generated surface gravity waves. *Atmos.-Ocean*, **27**, 210–236.
- Donelan, M. A., 1987: The effect of swell on the growth of wind waves. *Johns Hopkins APL Tech. Dig.*, **8**, 18–23.
- , 1990: Air–sea interaction. *The Sea*, B. LeMehaute and D. M. Hanes, Eds., Ocean Engineering Science, Vol. 9, John Wiley and Sons, 239–292.
- , 1998: Air–water exchange processes. *Physical Processes in Lakes and Oceans: Lake Biwa, Japan*, J. Imberger, Ed., Coastal Estuarine Series, Vol. 48, Amer. Geophys. Union, 18–36.
- , J. Hamilton, and W. H. Hui, 1985: Directional spectra of wind-generated waves. *Philos. Trans. Roy. Soc. London*, **315A**, 509–562.
- , M. Skafel, H. Graber, P. Liu, D. Schwab, and S. Venkatesh, 1992: On the growth rate of wind-generated waves. *Atmos.-Ocean*, **30**, 457–478.
- Dysthe, K. B., K. Trulsen, H. Krogstad, and H. Socquet-Juglard, 2003: Evolution of a narrow-band spectrum of random surface gravity waves. *J. Fluid Mech.*, **478**, 1–10.
- Ewans, K. C., 1998: Observations of the directional spectrum of fetch-limited waves. *J. Phys. Oceanogr.*, **28**, 495–512.
- Forrstall, G., 1981: Measurements of a saturated range in ocean wave spectra. *J. Geophys. Res.*, **86**, 8075–8084.
- Friehe, C. A., D. Khelif, and W. K. Melville, 2006: Aircraft air–sea flux measurements in the Gulf of Tehuantepec. Preprints, *14th Conf. on Interaction of the Sea and Atmosphere*, Atlanta, GA, Amer. Meteor. Soc., 7.2.
- Grachev, A. A., and C. W. Fairall, 2001: Upward momentum transfer in the marine boundary layer. *J. Phys. Oceanogr.*, **31**, 1698–1711.
- Hara, T., and S. Belcher, 2002: Wind forcing in the equilibrium range of wind-wave spectra. *J. Fluid Mech.*, **470**, 223–245.
- Hasselmann, D., M. Dunckel, and J. A. Ewing, 1980: Directional wave spectra observed during JONSWAP 1973. *J. Phys. Oceanogr.*, **10**, 1264–1280.
- Hasselmann, K., and Coauthors, 1973: Measurements of wind-wave growth and swell decay during the Joint North Sea Wave Project (JONSWAP). *Dtsch. Hydrogr. Z.*, **8**, 1–95.
- Holthuisen, L. H., 1983: Observations of the directional distribution of ocean wave energy. *J. Phys. Oceanogr.*, **13**, 191–207.
- Hwang, P. A., and D. W. Wang, 2001: Directional distributions and mean square slopes in the equilibrium and saturation ranges of the wave spectrum. *J. Phys. Oceanogr.*, **31**, 1346–1360.
- , —, E. J. Walsh, W. B. Krabill, and R. N. Swift, 2000a: Airborne measurements of the wavenumber spectra of ocean surface waves. Part I: Spectral slope and dimensionless spectral coefficient. *J. Phys. Oceanogr.*, **30**, 2753–2767.
- , —, —, —, and —, 2000b: Airborne measurements of the wavenumber spectra of ocean surface waves. Part II: Directional distribution. *J. Phys. Oceanogr.*, **30**, 2768–2787.
- Jackson, F. C., W. T. Walton, and P. L. Baker, 1985a: Aircraft and satellite measurement of ocean wave directional spectra using scanning-beam microwave radars. *J. Geophys. Res.*, **90**, 987–1004.
- , —, and C. Y. Peng, 1985b: A comparison of in situ and airborne radar observations of ocean wave directionality. *J. Geophys. Res.*, **90**, 1005–1017.
- Janssen, P. A. E. M., 1989: Wave-induced stress and the drag of air flow over sea waves. *J. Phys. Oceanogr.*, **19**, 745–754.
- , G. J. Komen, and W. J. P. de Voogt, 1987: Friction velocity scaling in wind wave generation. *Bound.-Layer Meteor.*, **38**, 29–35.
- Jones, I. S. F., and Y. Toba, 2001: *Wind Stress over the Ocean*. Cambridge University Press, 326 pp.
- Kahma, K. K., 1981: A study of the growth of the wave spectrum with fetch. *J. Phys. Oceanogr.*, **11**, 1505–1515.
- , and C. J. Calkoen, 1992: Reconciling discrepancies in the observed growth of wind-generated waves. *J. Phys. Oceanogr.*, **22**, 1389–1405.
- Kitaigorodskii, S. A., 1962: Applications of the theory of similarity to the analysis of wind-generated wave motion as a stochastic process. *Bull. Acad. Sci. USSR*, **1**, 105–117.
- , V. P. Krasitskii, and M. M. Zaslavskii, 1975: On Phillips' theory of equilibrium range in the spectra of wind-generated gravity waves. *J. Phys. Oceanogr.*, **5**, 410–420.
- Komen, G. J., S. Hasselmann, and K. Hasselmann, 1984: On the existence of a fully developed wind-sea spectrum. *J. Phys. Oceanogr.*, **14**, 1271–1285.
- Krabill, W. B., and C. F. Martin, 1987: Aircraft positioning using global positioning carrier phase data. *Navigation*, **34**, 1–21.
- , R. H. Thomas, K. Jezek, C. Kuivinen, and S. Manizade, 1995: Greenland ice sheet thickness changes measured by laser altimetry. *Geophys. Res. Lett.*, **22**, 2341–2344.
- Krogstad, H. E., 1990: Reliability and resolution of directional wave spectra from heave, pitch, and roll data buoys. *Directional Ocean Wave Spectra*, Johns Hopkins University Press, 66–71.
- Long, C. E., and D. T. Resio, 2007: Wind wave spectral observations in Currituck Sound, North Carolina. *J. Geophys. Res.*, **112**, C05001, doi:10.1029/2006JC003835.
- Melville, W. K., 1996: The role of surface-wave breaking in air–sea interaction. *Annu. Rev. Fluid Mech.*, **28**, 279–321.
- , and P. Matusov, 2002: Distribution of breaking waves at the ocean surface. *Nature*, **417**, 58–63.
- , L. Romero, and J. M. Kleiss, 2005: Extreme waves in the Gulf of Tehuantepec. *Rogue Waves: 14th 'Aha Huliko 'a Hawaiian*

- Winter Workshop, Honolulu, HI, University of Hawaii at Manoa, 23–28.
- Mitsuyasu, H., 1981: Directional spectra of ocean waves in generation area. *Proc. Conf. on Directional Wave Spectra Applications*, New York, NY, ASCE, 87–101.
- , 2002: A historical note on the study of ocean surface waves. *J. Oceanogr.*, **58**, 109–120.
- , F. Tasai, T. Suhara, S. Mizuno, M. Ohkusu, T. Honda, and K. Rikiishi, 1975: Observation of the directional wave spectra of ocean waves using a cloverleaf buoy. *J. Phys. Oceanogr.*, **5**, 750–760.
- Onorato, M., A. R. Osborne, M. Serio, D. Resio, A. N. Pushkarev, V. E. Zakharov, and C. Brandini, 2002: Freely decaying weak turbulence for sea surface gravity waves. *Phys. Rev. Lett.*, **89**, 144501, doi:10.1103/PhysRevLett.89.144501.
- Perrie, W., and B. Toulany, 1990: Fetch relations for wind-generated waves as a function of wind-stress scaling. *J. Phys. Oceanogr.*, **20**, 1666–1681.
- Phillips, O. M., 1958: The equilibrium range in the spectrum of wind-generated waves. *J. Fluid Mech.*, **4**, 426–433.
- , 1977: *The Dynamics of the Upper Ocean*. Cambridge University Press, 336 pp.
- , 1981: The dispersion of short wavelets in the presence of a dominant long wave. *J. Fluid Mech.*, **107**, 465–485.
- , 1985: Spectral and statistical properties of the equilibrium range in wind-generated gravity waves. *J. Fluid Mech.*, **156**, 505–531.
- Pushkarev, A., D. Resio, and V. Zakharov, 2003: Weak turbulent approach to the wind-generated gravity sea waves. *Physica D*, **184**, 29–63.
- Rascles, N., F. Ardhuin, P. Queffelecoul, and D. Croize-Fillon, 2008: A global parameter database for geophysical applications. Part 1: Wave-current-turbulence interaction parameters for the open ocean based on traditional parameterizations. *Ocean Modell.*, **25**, 154–171.
- Resio, D. T., C. E. Long, and C. L. Vincent, 2004: The equilibrium-range constant in wind-generated wave spectra. *J. Geophys. Res.*, **109**, C01018, doi:10.1029/2003JC001788.
- Romero, L., 2008: Airborne observations and numerical modeling of fetch-limited waves in the Gulf of Tehuantepec. Ph.D. thesis, University of California, San Diego, 111 pp.
- , and W. K. Melville, 2010: Numerical modeling of fetch-limited waves in the Gulf of Tehuantepec. *J. Phys. Oceanogr.*, **40**, 466–486.
- Romero-Centeno, R., J. Zavala-Hidalgo, A. Gallegos, and J. O'Brien, 2003: Isthmus of Tehuantepec wind climatology and ENSO signal. *J. Climate*, **16**, 2628–2639.
- Schule, J. J., L. S. Simpson, and P. S. DeLeonibus, 1971: A study of wave spectra with an airborne laser. *J. Geophys. Res.*, **76**, 4160–4171.
- Schultz, D. M., W. E. Bracken, and L. F. Bosart, 1998: Planetary- and synoptic-scale signatures associated with Central American cold surges. *Mon. Wea. Rev.*, **126**, 5–27.
- Smith, W. H. F., and D. T. Sandwell, 1997: Global seafloor topography from satellite altimetry and ship depth soundings. *Science*, **277**, 1957–1962.
- Socquet-Juglard, H., K. Dysthe, K. Trulsen, H. E. Krodstad, and J. D. Liu, 2005: Probability distributions of surface gravity waves during spectral changes. *J. Fluid Mech.*, **542**, 195–216.
- Steenburgh, W. J., D. M. Schultz, and B. A. Colle, 1998: The structure and evolution of gap outflow over the Gulf of Tehuantepec, Mexico. *Mon. Wea. Rev.*, **126**, 2673–2691.
- Sverdrup, H. U., and W. H. Munk, 1947: Wind, sea, and swell: Theory of relations for forecasting. U. S. Hydrographic Office Tech. Rep. 601, 44 pp.
- Toba, Y., 1973: Local balance in the air-sea boundary process. *J. Oceanogr. Soc. Japan*, **29**, 209–220.
- Violante-Carvalho, N., F. Ocampo-Torres, and I. Robinson, 2004: Buoy observations of the influence of swell on wind waves in the open ocean. *Appl. Ocean Res.*, **26**, 49–60.
- Walsh, E. J., D. W. Hancock, D. E. Hines, R. N. Swift, and J. F. Scott, 1985: Directional wave spectra measured with the surface contour radar. *J. Phys. Oceanogr.*, **15**, 566–592.
- Wang, D. W., and P. A. Hwang, 2001: Evolution of the bimodal directional distribution of ocean waves. *J. Phys. Oceanogr.*, **31**, 1200–1221.
- WISE Group, 2007: Wave modelling—The state of the art. *Prog. Oceanogr.*, **75**, 603–674.
- Wu, J., 1982: Wind-stress coefficients over sea surface from breeze to hurricane. *J. Geophys. Res.*, **87**, 9704–9706.
- Wyatt, L. R., 1995: The effect of fetch on the directional spectrum of Celtic Sea storm waves. *J. Phys. Oceanogr.*, **25**, 1550–1559.
- Young, I. R., 1995: The determination of confidence limits associated with estimates of the spectral peak frequency. *Ocean Eng.*, **22**, 669–686.
- , 1998: An experimental investigation of the role of atmospheric stability in wind wave growth. *Coastal Eng.*, **34**, 23–33.
- , 1999: *Wind Generated Ocean Waves*. Elsevier Science, 288 pp.
- , S. Hasselmann, and K. Hasselmann, 1987: Computations of the response of a wave spectrum to a sudden change in wind direction. *J. Phys. Oceanogr.*, **17**, 1317–1338.
- , L. A. Verhagen, and M. L. Banner, 1995: A note on the bimodal directional spreading of fetch-limited wind waves. *J. Geophys. Res.*, **100**, 773–778.
- Zakharov, V. E., and N. N. Filonenko, 1967: Energy spectrum for stochastic oscillations of the surface of a liquid. *Sov. Phys. Dokl.*, **11**, 881–883.